$7

QEX

September/October 2019

www.arrl.org

A Forum for Communications Experimenters

Issue No. 316

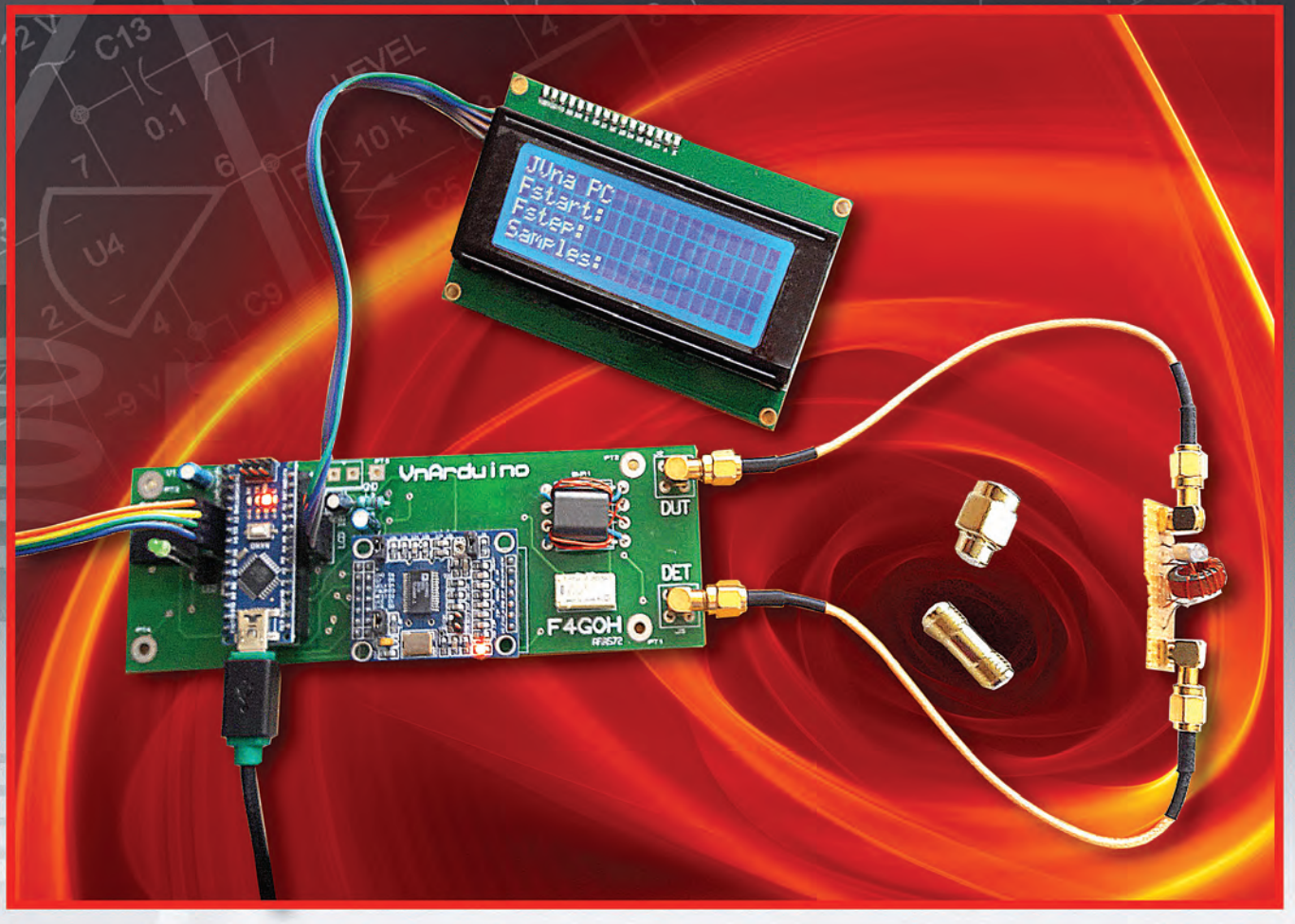

MØTCC explains inductor losses in Pi networks.

ARRL The national association for AMATEUR RADIO™
225 Main Street
Newington, CT USA 06111-1494

KENWOOD

3rd IMDR 110 dB*

RMDR 122 dB*

BDR 150 dB*

Performance Exceeding Expectations.

The most happy and sublime encounters happen in the worst circumstances and under the harshest conditions.

There are enthusiasts who know this all too well because of their love of HF radio.

Results born of certainty and not circumstance. Delivered through impeccable performance. This is our offering to you.

"The Kenwood TS-890S has the highest RMDR of any radio I have ever measured."
- Rob Sherwood - NC0B - December 2018

HF/50MHz TRANSCEIVER

TS-890S

NEW

Top-class receiving performance

3 kinds of dynamic range make for top-class performance.

- Third order intermodulation Dynamic Range (3rd IMDR) 110dB*
- Reciprocal Mixing Dynamic Range (RMDR) 122dB*
- Blocking Dynamic Range (BDR) 150dB*

*Values are measured examples. (2kHz spacing:14.1 MHz, CW, BW 500 Hz, Pre Amp OFF)

- Full Down Conversion RX
- High Carrier to Noise Ratio 1st LO
- H-mode mixer

4 kinds of built-in roofing filters

500Hz / 2.7kHz / 6kHz / 15kHz (270Hz Option)

7 inch Color TFT Display

- Roofing frequency sampling band scope
- Band scope auto-scroll mode
- Multi-information display including filter scope

Clean and tough 100W output

Built-in high-speed automatic antenna tuner

32-bit floating-point DSP for RX / TX and Bandscope

Customer Support: (310) 639-4200

www.kenwood.com/usa

ISO9001 Registered
JVCKENWOOD Corporation

ADS#02119

QEX

QEX (ISSN: 0886-8093) is published bimonthly in January, March, May, July, September, and November by the American Radio Relay League, 225 Main St., Newington, CT 06111-1494. Periodicals postage paid at Hartford, CT and at additional mailing offices.

POSTMASTER: Send address changes to: QEX, 225 Main St., Newington, CT 06111-1494 Issue No 316

Publisher
American Radio Relay League

Kazimierz "Kai" Siwiak, KE4PT
Editor

Lori Weinberg, KB1EIB
Assistant Editor

Zack Lau, W1VT
Ray Mack, W5IFS
Contributing Editors

Production Department

Steve Ford, WB8IMY
Publications Manager

Michelle Bloom, WB1ENT
Production Supervisor

Sue Fagan, KB1OKW
Graphic Design Supervisor

David Pingree, N1NAS
Senior Technical Illustrator

Brian Washing
Technical Illustrator

Advertising Information Contact:

Janet L. Rocco, W1JLR
Business Services
860-594-0203 – Direct
800-243-7768 – ARRL
860-594-4285 – Fax

Circulation Department

Cathy Stepina, *QEX Circulation*

Offices

225 Main St., Newington, CT 06111-1494 USA
Telephone: 860-594-0200
Fax: 860-594-0259 (24 hour direct line)
e-mail: **qex@arrl.org**

Subscription rate for 6 issues:

In the US: $29;

US by First Class Mail: $40;

International and Canada by Airmail: $35

Members are asked to include their membership control number or a label from their QST when applying.

In order to ensure prompt delivery, we ask that you periodically check the address information on your mailing label. If you find any inaccuracies, please contact the Circulation Department immediately. Thank you for your assistance.

About the Cover

Tuck Choy, MØTCC, considers inductor losses in Pi networks in this second and final part of his series. He discusses the T-matrix formulation, as well as its use to develop the response functions for the Pi network, and presents an analysis of the exact and approximate results for bandwidth and harmonics suppression predictions. Choy also presents some preliminary experimental measurements using an Arduino-based vector network analysis system.

In This Issue

Features

Index of Advertisers

The American Radio Relay League

The American Radio Relay League, Inc, is a noncommercial association of radio amateurs, organized for the promotion of interest in Amateur Radio communication and experimentation, for the establishment of networks to provide communications in the event of disasters or other emergencies, for the advancement of the radio art and of the public welfare, for the representation of the radio amateur in legislative matters, and for the maintenance of fraternalism and a high standard of conduct.

ARRL is an incorporated association without capital stock chartered under the laws of the state of Connecticut, and is an exempt organization under Section 501(c)(3) of the Internal Revenue Code of 1986. Its affairs are governed by a Board of Directors, whose voting members are elected every three years by the general membership. The officers are elected or appointed by the Directors. The League is noncommercial, and no one who could gain financially from the shaping of its affairs is eligible for membership on its Board.

"Of, by, and for the radio amateur," ARRL numbers within its ranks the vast majority of active amateurs in the nation and has a proud history of achievement as the standard-bearer in amateur affairs.

A *bona fide* interest in Amateur Radio is the only essential qualification of membership; an Amateur Radio license is not a prerequisite, although full voting membership is granted only to licensed amateurs in the US.

Membership inquiries and general correspondence should be addressed to the administrative headquarters:

ARRL
225 Main St.
Newington, CT 06111 USA
Telephone: 860-594-0200
FAX: 860-594-0259 (24-hour direct line)

Officers

President: Rick Roderick, K5UR
P.O. Box 1463, Little Rock, AR 72203

Chief Executive Officer: Howard Michel, WB2ITX

The purpose of *QEX* is to:

1) provide a medium for the exchange of ideas and information among Amateur Radio experimenters,

2) document advanced technical work in the Amateur Radio field, and

3) support efforts to advance the state of the Amateur Radio art.

All correspondence concerning *QEX* should be addressed to the American Radio Relay League, 225 Main St., Newington, CT 06111 USA. Envelopes containing manuscripts and letters for publication in *QEX* should be marked Editor, *QEX*.

Both theoretical and practical technical articles are welcomed. Manuscripts should be submitted in word-processor format, if possible. We can redraw any figures as long as their content is clear. Photos should be glossy, color or black-and-white prints of at least the size they are to appear in *QEX* or high-resolution digital images (300 dots per inch or higher at the printed size). Further information for authors can be found on the Web at **www.arrl.org/qex/** or by e-mail to **qex@arrl.org**.

Kazimierz "Kai" Siwiak, KE4PT

Perspectives

Style Changes Coming to *QEX*

You will soon see some style changes phased into future *QEX* articles. For improved readability, **Notes** will no longer use difficult-to-read superscripts in the article or in the list of Notes. Instead, Notes will be identified by sequential numbers surrounded by square brackets, as in "see **[1]**", with the first occurrence in bold typeface. Subsequent mentions of the same Note will be in plain text surrounded by square brackets. The list of Notes at the end of the article will be numbers in square brackets followed by a single space.

To help readers locate descriptions of Figures and Tables in the article, the first mention of a Figure or a Table will use a bold typeface, such as **Figure 1** and **Table 1**. Subsequent mentions to the same Figure or Table will use plain text.

As time goes on we may implement additional style changes that will help further improve readability. We'd like your feedback.

In This Issue

Tuck Choy, MØTCC, considers inductor losses in Pi networks in the final part of his series.

Darrel Emerson, AA7FV, examines the polarizations of modestly-sized square loop antennas.

Ulrich Rohde, N1UL, and Kai Siwiak, KE4PT, examine tuning of short antennas for portable operations.

Maynard Wright, W6PAP, uses *Octave* for complex characteristic impedance calculations.

Writing for *QEX*

Keep the full-length *QEX* articles flowing in, or share a **Technical Note** of several hundred words in length plus a figure or two. Let us know that your submission is intended as a **Note**. *QEX* is edited by Kazimierz "Kai" Siwiak, KE4PT, (**ksiwiak@arrl.org**) and is published bimonthly. *QEX* is a forum for the free exchange of ideas among communications experimenters. The content is driven by you, the reader and prospective author. The subscription rate (6 issues per year) in the United States is $29. First Class delivery in the US is available at an annual rate of $40. For international subscribers, including those in Canada and Mexico, *QEX* can be delivered by airmail for $35 annually. Subscribe today at **www.arrl.org/qex**.

Would you like to write for *QEX*? We pay $50 per published page for articles and Technical Notes. Get more information and an Author Guide at **www.arrl.org/qex-author-guide**. If you prefer postal mail, send a business-size self-addressed, stamped (US postage) envelope to: *QEX* Author Guide, c/o Maty Weinberg, ARRL, 225 Main St, Newington, CT 06111.

Very best regards,

Kazimierz "Kai" Siwiak, KE4PT

Tuck Choy, MØTCC

18 Rue de L'Arnede, Montagnac 34530, France; **tuckvk3cca@gmail.com**

Pi Networks With or Without Inductor Loss — Part 2

Network analysis — a tale with fewer Qs.

In this final part, I discuss the *T*-matrix formulation, its use to develop the response functions for the Pi network and an analysis of the exact and approximate results for bandwidth and harmonics suppression predictions. Some preliminary experimental measurements will be shown using an Arduino based VNA system.

1. Introduction

In the previous article[1] I developed the formulas for the design or synthesis of Pi networks with several design options. In this article I shall conclude by looking at the network characteristics once a design has been made, with consideration of several termination conditions. This plays a significant part in determining the network response characteristics. I will show two ways to present the formulas, either in the minimal parameters *Q* format or in component values format. However, please note that these formulas agree only if the solutions are exact, and for experiments the latter is more appropriate but they do contain more parameters.

2. T Matrix Formulation for Transfer Functions

In this Section I shall first set up the *T*-matrix formulas for the calculation of the various response and impedance functions over all frequencies. Although one can in principle obtain some of these response functions by direct circuit analysis, the use of the *T*-matrix method is by far more elegant and systematic. It is in fact indispensable for calculating the impedance functions under iterative or image impedance operation conditions as required here. For details of the method see for example Terman[2], Valkenberg[3] and Skilling[4], or for an introduction see Hayward[5]. In general, it is by no means a simple task in calculations to ensure that iterative or image conditions are satisfied without the *T*-matrix formulation, see Figure 1. In general $A \neq D$ except for a symmetric network.

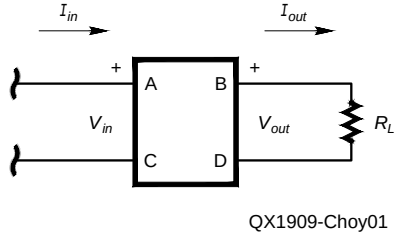

Figure 1 — A two port network terminated in a load resistance R_L, with the voltage and current conventions for defining the *T* matrix.

With the *T* matrix as defined in Figure 1, the network equations are:

$$V_{in} = AV_{out} + B\,I_{out}$$
$$I_{in} = CV_{out} + D\,I_{out} \qquad (1)$$

For an output terminated with a load resistance R_L Eqn (1) shows that:

$$V_{in} = AV_{out} + B\frac{V_{out}}{R_L}$$
$$I_{in} = CV_{out} + D\,\frac{V_{out}}{R_L}\ . \qquad (2)$$

In this case, we can immediately write down the various impedance functions:

$$Z_{11} = \frac{V_{in}}{I_{in}} = \frac{A + \dfrac{B}{R_L}}{C + \dfrac{D}{R_L}} \qquad (3a)$$

$$Z_{12} = \frac{V_{in}}{I_{out}} = AR_L + B \qquad (3b)$$

$$Z_{21} = \frac{V_{out}}{I_{in}} = \frac{1}{C + \dfrac{D}{R_L}} \qquad (3c)$$

$$Z_{22} = \frac{V_{out}}{I_{out}} = R_L \qquad (3d)$$

Note that these impedances Z_{ij} are not all independent because $Z_{12}Z_{21} = Z_{11}Z_{22}$ due to the fact that for a linear passive network the determinant $\Delta = (AD - BC) = 1$, see for example [*op. cit.*[4, 5]]. I shall give my proof in Appendix 1. To obtain the gain transfer functions we need to specify input conditions. For a constant ideal voltage generator input, it follows that the generic voltage transfer function H_T is given by:

$$H_T = \frac{V_{out}}{V_{in}} = \frac{1}{A + \dfrac{B}{R_L}}\ . \qquad (4)$$

However, for a constant ideal current generator input, the generic current transfer function H_I is now given by:

$$H_I = \frac{I_{out}}{I_{in}} = \frac{1}{C\,R_L + D}\ . \qquad (5)$$

Neither of these input conditions are satisfied in practice without special experimental arrangements and for connecting to power amplifier outputs, the constant current generator is a useful approximation as mentioned in Part 1, being a match for maximum power output. Nevertheless from the *T*-matrix formulation we can conclude that for purely reactive networks, the gain transfer functions Eqns (4) and (5) are of an all-pole type whereas the impedance functions Eqn (3) can have both poles and zeros in accordance with Forster's theorem as mentioned in Part 1. For linear passive networks, we also have the useful condition that the determinant $\Delta = 1$ mentioned above. This is often a useful check that we got things written down correctly. In the next section we will commence the task of finding the *T* matrix for the Pi network from which all the quantities above can be evaluated.

3. Basic T Matrices for the Pi Network

The power of the *T*-matrix method is that for cascaded networks the resultant *T* matrix is the matrix product of the *T* matrices of the individual networks, see for example Hayward [*op. cit.*[5]]. So, we shall start with the two basic building blocks, see Figures 2 and 3, which are the left-handed and right-handed *L* networks. From either of these networks we can get the *T* matrix for a single series impedance by taking $Y = 0$, or a shunt admittance by taking $Z = 0$ so these are special limits. Figure 2 and Figure 3 are standard text book results that will be useful to us, see for example [*op. cit.*[3,4,5]]. However, for the benefit of the reader, I have also provided a sketch of the proofs in Appendix 1.

With the above results as given we can now write down immediately the *T* matrix for the Pi network of Figure 4

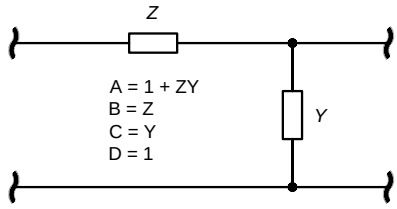

Figure 2 — The left-handed L network with its T matrix components. Z is the series impedance and Y is the shunt admittance.

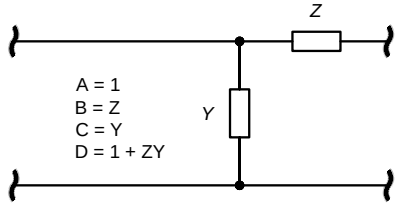

Figure 3 — The right-handed L network with its T matrix components. Z is the series impedance and Y is the shunt admittance.

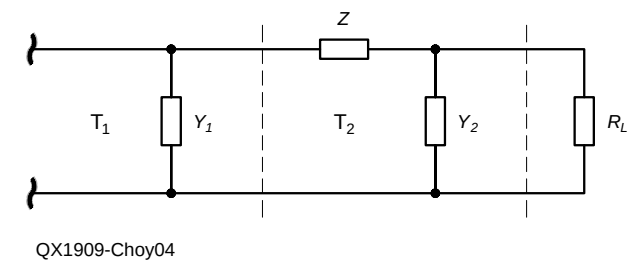

Figure 4 — Pi network (singly terminated) whose *T* matrix can be obtained from that of Figure 2 and Figure 3 by matrix product $T = T_1T_2$ see Eqn (6). The vertical dash lines show my choice of partitioning, which is one of several choices.

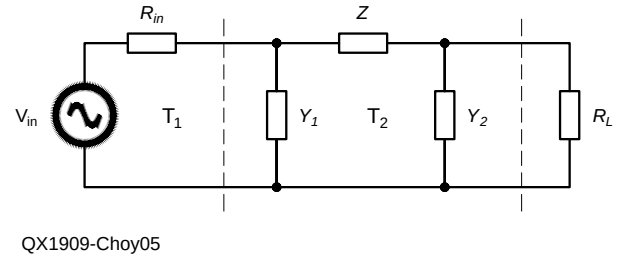

Figure 5 — Doubly terminated Pi network whose *T* matrix can be obtained from that of Figure 2 and Figure 4 by matrix product $T = T_1T_2$ see Eqn (7). The vertical dash lines show my choice of partitioning, which in this case consists of a series resistance R_{in} cascaded with the Pi network of Figure 4. R_{in} could represent the internal resistance of a voltage generator connected to the input as in this example.

$$\begin{aligned} T_{\pi 1} &= T_1 T_2 \\ &= \begin{pmatrix} 1 & 0 \\ Y_1 & 1 \end{pmatrix} \begin{pmatrix} 1+ZY_2 & Z \\ Y_2 & 1 \end{pmatrix} \\ &= \begin{pmatrix} 1+ZY_2 & Z \\ Y_1+Y_2+ZY_1Y_2 & 1+ZY_1 \end{pmatrix}. \end{aligned} \tag{6}$$

Now we are in business to obtain all the impedance and transfer functions for the singly terminated network of Figure 4. However, we must also consider the case of double termination, see Figure 5. In this case the Pi-network *T* matrix can be easily obtained from the *T* matrix of a series terminating resistance R_{in} from Figure 2 multiplied by the *T* matrix of Eqn (6). Thus, we have for Figure 5:

$$\begin{aligned} T_{\pi\, term} &= T_1 T_2 \\ &= \begin{pmatrix} 1 & R_{in} \\ 0 & 1 \end{pmatrix} \begin{pmatrix} 1+ZY_2 & Z \\ Y_1+Y_2+ZY_1Y_2 & 1+ZY_1 \end{pmatrix} \\ &= \begin{pmatrix} 1+ZY_2+R_{in}Y_\pi & Z+R_{in}+ZR_{in}Y_1 \\ Y_\pi & 1+ZY_1 \end{pmatrix} \end{aligned} \tag{7}$$

where $Y_\pi = Y_1 + Y_2 + ZY_1Y_2$.

Note the power of the *T*-matrix method and the complexity introduced by the extra termination. The partitioning may be done differently but this seems to be the most straightforward.

4. Impedance and Voltage Transfer functions

We can now write down the general formulas for impedance and voltage transfer functions of these Pi networks by substituting their appropriate *ABCD* coefficients in the defining Eqns (3) – (5). For the rest of this article I shall not pay much attention to the impedance functions so I shall just show that Z_{11} is indeed given by Eqn (14) of Part 1. Given the *ABCD* coefficients of Eqn (6), we can immediate write down Z_{11} from Eqn (3) as:

$$\begin{aligned} Z_{11} &= \frac{A+\dfrac{B}{R_L}}{C+\dfrac{D}{R_L}} \\ &= \frac{1+ZY_2+\dfrac{Z}{R_L}}{Y_1+Y_2+ZY_1Y_2+\dfrac{(1+ZY_1)}{R_L}}. \end{aligned} \tag{8}$$

Now, we have the following values for impedance $Z = pL$ and admittances: $Y_1 = pC_1$ and $Y_2 = pC_2$ where I have changed the Laplace complex frequency to p instead of z as used in Eqn (14) of Part 1 to avoid confusion. Now Eqn (8) becomes:

$$Z_{11}(p) = \frac{1 + \frac{pL}{R_L} + p^2 LC_2}{\frac{1}{R_L} + p(C_1 + C_2) + \frac{p^2 LC_1}{R_L} + p^3 LC_1 C_2} \quad . \tag{9}$$

From here the reader can easily verify that Eqn (9) and Eqn (14) of Part 1 are identical, by using the definitions given after Eqn (14), demonstrating the power of the *T*-matrix method. Let me now concentrate on the transfer functions Eqns (4) and (5). There are in fact three such functions that I shall be looking at: Eqn (4) which is the generic singly terminated voltage transfer function H_T valid when the network is connected directly to an ideal voltage source of zero or infinitely low internal resistance. Then we have the constant current transfer function Eqn (5): H_I also singly terminated and finally the doubly terminated voltage transfer function H_{term} which is based on the *T* matrix of Figure 5. The first one is in fact the simplest, and we can get a lot out of it analytically. From Eqns (4) and (6) we have:

$$\begin{aligned} H_T^0(p) &= \frac{1}{A + \frac{B}{R_L}} \\ &= \frac{1}{1 + ZY_2 + \frac{Z}{R_L}} \\ &= \frac{1}{1 + \frac{pL}{R_L} + p^2 LC_2} . \end{aligned} \tag{10}$$

Notice immediately that the poles of these function are the zeros of Z_{11} and I have now followed the convention in Part 1 to put a superscript 0 for the lossless case. Replacing $Z = pL + r_L$ in the above Eqn (10), we get the voltage transfer function for the lossy inductor case, now dropping the superscript 0:

$$H_T(p) = \frac{1}{1 + \frac{r_L}{R_L} + p\left(r_L C_2 + \frac{L}{R_L}\right) + p^2 LC_2} \quad . \tag{11}$$

Eqns (10) and (11) can be used as they are for our analysis, but we must bear in mind that the reactive component values differ in the two cases — I have refrained from putting too many superscript 0's in Eqn (10) to avoid clutter. To rewrite these response functions in terms of the design parameters, we must first normalize the frequency to ω_0 the design resonance frequency so that: $p = s\omega_0$ then using the following expressions in Part 1, which are still valid in the lossy inductor case

$\frac{\omega_0 L}{R_L} = \frac{X_L}{R_L} = \frac{Q_U}{1 + Q_2^2}$ and $\omega_0^2 LC_2 = \frac{Q_U Q_2}{1 + Q_2^2}$. We now have:

$$\begin{aligned} H_T(s) &= \frac{1}{1 + \frac{r_L}{R_L} + s\left(Q_2 \frac{r_L}{R_L} + \frac{X_L}{R_L}\right) + \frac{s^2}{\alpha_2}} \\ &= \frac{\alpha_2}{\alpha_2\left(1 + \frac{r_L}{R_L}\right) + s\frac{q_2}{Q_2} + s^2} \end{aligned} \tag{12}$$

where

$$\alpha_2 = \frac{1 + Q_2^2}{Q_U Q_2} \;,\; q_2 = 1 + \frac{Q_2}{Q_L}$$

and we have used: $Q_L = X_L/r_L$. This equation can be further simplified by judicious use of expressions for the *Q* parameters given in Part 1, and we then have:

$$H_T(s) = \frac{\varepsilon\left(1 + Q_2^2\right)}{1 + \varepsilon Q_2^2 + s(Q_1 + Q_2) + s^2 \varepsilon Q_U Q_2} \tag{13}$$

Similarly, using Eqns (4)-(7), I can also derive the constant current transfer function $H_I(s)$ and the doubly-terminated voltage transfer function $H_{term}(s)$ in the same way for the general lossy case. For convenience, I shall express these generic functions as:

$$H_X(s) = \frac{\alpha_H}{a + sb + s^2 c + s^3 d} \quad . \tag{14}$$

The coefficients α_H, *a*, *b*, *c* and *d* are now tabulated in Table 1 and the subscript *x* is used to indicate the specific transfer function, for example *x* is *T*, *I* or *term*.

We can also write $\varepsilon Q_U = Q_{Net} = Q_1 + \varepsilon Q_2$, which follows from Eqns (26) and (39) of Part 1 if we so desire. I found this relation invaluable to prove that all the power transfer functions have the same value ε at resonance, see below. To obtain $H_{term}(s)$, the last row of Table 1, I have used Eqns (4) and (7) with $R_{in} = R_s$ the input image resistance. To recover the lossless inductor case, we can just take $\varepsilon \to 1$ and replace the *Q*s to those for the lossless components, namely, with superscript 0. As you can see, both $H_I(s)$ and $H_{term}(s)$ contain cubic poles, which means more work is needed to calculate the bandwidth exactly, see later. From these equations I can now write down the power gain transfer functions. These are given by the relations:

$$G_T(j\omega) = \frac{R_s}{R_L}\left|H_T(j\omega)\right|^2 \tag{15a}$$

$$G_I(j\omega) = \frac{R_L}{R_s}\left|H_I(j\omega)\right|^2 \tag{15b}$$

and

$$G_{term}(j\omega) = \frac{4R_s}{R_L}\left|H_{term}(j\omega)\right|^2 \tag{15c}$$

Here I have moved from the complex *s* plane to the *j*ω frequency axis. For the expression R_s/R_L see Eqn (29) in Part 1. Again, for convenience, I have tabulated the parameters for these equations in Table 2 for easy reference. These power-gain functions are defined so that at resonance $\omega = 1$ we get $G_T(j) = G_I(j) = G_{term}(j) = \varepsilon$ as mentioned. These results can be algebraically proven from the formulas in Table 2, for an example, see below. The generic formula for $G_x(j\omega)$ from Eqns (14) and (15) is given by:

$$G_x(j\omega) = \frac{\alpha_G}{\left(a_G - \omega^2 b_G\right)^2 + \omega^2\left[c_G + d_G\left(1 - \omega^2\right)\right]^2} \quad . \tag{16}$$

Coefficients α_G, a_G, b_G, c_G and d_G are given in Table 2. As can be seen, the power transfer functions are all functions of only three design parameters, namely and Q_1, Q_2 , and Q_L, since the quantities ε and Q_U in Table 2 are functions of just these three parameters, see Eqns (30) and (39) in Part 1. At this point I shall use Eqn (12) to prove the very important voltage phase relation Eqn (42) in Part 1. First, I

shall show an example of how the power gain function reduces to ε at the design frequency. From Eqn (16) we have $G_T(j\omega)$ for ω = 1 thus:

$$G_T(j) = \frac{\varepsilon\left(1+Q_1^2\right)\left(1+Q_2^2\right)}{\left(1+\varepsilon Q_2^2 - \varepsilon Q_U Q_2\right)^2 + \left[Q_1+Q_2,\right]^2} \qquad (17)$$
$$= \varepsilon$$

where use is made of the useful relation $\varepsilon Q_U = Q_{Net} = Q_1 + \varepsilon Q_2$, as mentioned earlier. In a similar way, the reader can also derive the other important normalization results: $G_I(j) = G_{term}(j) = G_T(j) = \varepsilon$ mentioned earlier.

Now from Eqn (12) by rationalization we can obtain:

$$H_T(j) = \frac{\alpha_2}{\gamma_2^2 + \left(\frac{q_2}{Q_2}\right)^2}\left(\gamma_2 - j\frac{q_2}{Q_2}\right) \qquad (18)$$
$$= \left|H_T(j)\right| e^{-j\beta}$$

where

$$\gamma_2 = \alpha_2\left(1+\frac{r_L}{R_L}\right) - 1$$

and β is the phase angle at the designed resonance frequency when ω = 1. This implies that:

$$\sin\beta = \left|H_T(j)\right|\frac{q_2}{\alpha_2 Q_2} \qquad (19)$$
$$= \left|H_T(j)\right|\frac{q_2 X_L}{R_L} \quad .$$

The last step follows from Eqn (25) of Part 1, also mentioned above after Eqn (11). Using $|H_T(j)|^2 = \frac{\varepsilon R_L}{R_s}$ and Eqn (29) of Part 1 we then have:

$$\sin\beta = \sqrt{\frac{\varepsilon R_L}{R_s}}\frac{q_2 Q_U}{1+Q_2^2} \qquad (20)$$
$$= \frac{Q_1+Q_2}{\sqrt{\left(1+Q_1^2\right)\left(1+Q_2^2\right)}} \quad .$$

This proves Eqn (42) in Part 1 and also provides a further simplification given by the last part of Eqn (20), which is an easier way to calculate the phase angle. From here in the first part taking $\varepsilon \to 1$ and $q_2 \to 1$ gives the basis for the phase-based design formulas for the lossless inductors, see Eqn (15) to (17) in Part 1.

Finally it is important to note that the transfer functions given in Eqn(14) with Table 1 and Eqn (16) with Table 2 are design parameters based, i.e., and Q_1, Q_2 , and Q_L are the three fundamental parameters. Corresponding equations can also be derived which are components-based i.e. in terms of and X_{C1}, X_{C2}, X_L, R_L, R_s, and Q_L or r_L. For convenience I have tabulated the parameters for Eqns (14) and (16) in the Appendix 2. Together they provide the equations for the network analysis given the circuit component values. While curves plotted from these two sets of equations should give identical results if no approximations are used as in the lossless model — see column 2 in Table 1 of Part 1 — and the exact lossy model — see column 6 in Table 1 of Part 1 — this will not be the case when approximations such as those discussed in Part 1 were used — see column 3 to 5 in Table 1 of Part 1. The *Q*-parameters based equations are better for use in modeling the response during design since they focus correctly on the three main fundamental *Q* parameters, which alone control the network response. On the other hand, the components-based equations should be used once a design is settled or for empirical studies. The agreement between the response curves from these two sets of equations for the exact lossy model is most notable as it requires getting the phase angle β to be correct as discussed in Part 1 — see row 2 in Table 1 of Part 1. The reader can readily verify this independently.

5. Power Gain, Bandwidth, Harmonic Suppression

5.1. Power gain response

We can now plot the response functions, say from dc to an octave in frequency above the fundamental. I shall start by using the *Q*-based formulas to plot the power gain transfer functions $G_T(j\omega)$, $G_I(j\omega)$ and $G_{term}(j\omega)$. Without loss of generality I shall plot the curves for an asymmetric Pi network model using data from Table 1 of Part 1, for there is no exact solution for a symmetric network that has $Q_1 = Q_2$with a finite Q_L, see Eqns (29), (30), (39) and (40) in Part 1. In Figure 6, I have plotted $G_T(j\omega)$ which at ω = 1 gives the exact insertion loss of 1.87 dB for the lossy curve (Q_L = 12) as required. From Eqn (16), at dc the value of $G_T(0) = \alpha_G/(a_G)^2$ while at high frequencies $\omega \to \infty$, $G_T(j\omega) \sim \alpha_G/(\omega^2 b_G)^2$ where the coefficients are given by row 1 of Table 2. Note that the peaks of these curves are at frequencies lower than the design resonance frequency. The exact peak frequency can be calculated from Eqn (16) if desired by elementary calculus. Also, as we shall see later the exact "bandwidth" can be calculated by solving a quadratic equation. Next in Figure 7, I have plotted $G_I(j\omega)$ which at ω = 1 again gives the exact insertion loss of 1.87 dB for the lossy

Table 1.

Coefficients α_H, a, b, c, and d for $H_x(s)$ in Eqn (14).

$x = T$	$\alpha_H = \varepsilon(1+Q_2^2), a = 1+\varepsilon Q_2^2, b = Q_1+Q_2, c = \varepsilon Q_U Q_2, d = 0$
$x = I$	$\alpha_H = a = (1+Q_1^2), b = Q_1+Q_2+d, c = Q_1(Q_1+Q_2), d = \varepsilon Q_U Q_1 Q_2$
$x = term$	$\alpha_H = \varepsilon(1+Q_2^2), a = 2+Q_1^2+\varepsilon Q_2^2, b = 2(Q_1+Q_2)+d, c = \varepsilon Q_U(Q_1+Q_2), d = \varepsilon Q_U Q_1 Q_2$

Table 2.

Coefficients α_G, a_G, b_G, c_G, and d_G for $G_x(j\omega)$ in Eqn (16). With these functions we can calculate exactly a given -*y* dB point from the design resonance frequency and the harmonic suppression characteristics, see text. The angular frequency ω is here normalized to the design frequency.

$x = T$	$\alpha_G = \varepsilon(1+Q_1^2)(1+Q_2^2), a_G = 1+\varepsilon Q_2^2, b_G = \varepsilon Q_U Q_2, c_G = Q_1+Q_2, d_G = 0$
$x = I$	$\alpha_G = \varepsilon(1+Q_1^2)(1+Q_2^2), a_G = 1+Q_1^2, b_G = Q_1(Q_1+Q_2), c_G = Q_1+Q_2, d_G = \varepsilon Q_U Q_1 Q_2$
$x = term$	$\alpha_G = 4\,\varepsilon(1+Q_1^2)(1+Q_2^2), a_G = 2+Q_1^2+\varepsilon Q_2^2, b_G = \varepsilon Q_U(Q_1+Q_2)+(1-\varepsilon)Q_1 Q_2, c_G = 2(Q_1+Q_2), d_G = \varepsilon Q_U Q_1 Q_2$

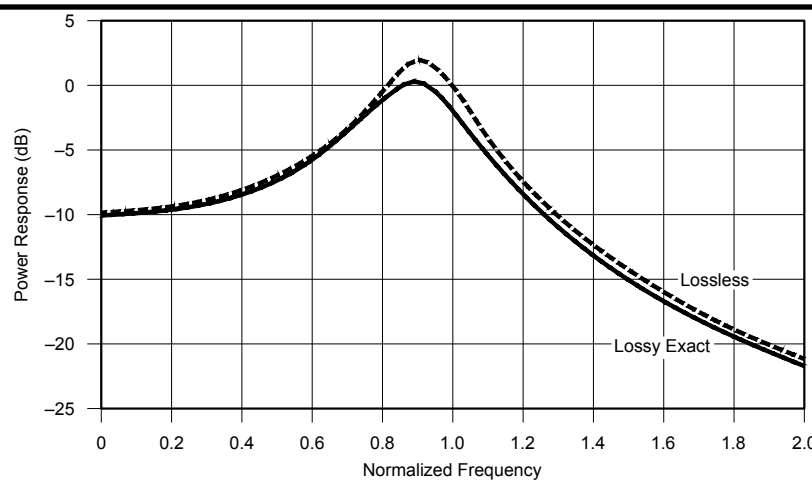

Figure 6 — Universal power response function $G_T(j\omega)$ in dB from Eqn (16) and row 1 of Table 2 for the model parameters given in Table 1 of Part 1. The dashed line is for the lossless model with $Q_1 = 0.942$ and $Q_2 = 4.229$ while the solid curve is the lossy model with $Q_1 = 0.872$, and $Q_2 = 5.105$ and $Q_L = 12$. Note that these functions peak at a frequency $\omega < 1$ and the concept of a bandwidth at $\omega = 1$ analogous to a conventional resonance circuit is therefore inappropriate. Nevertheless, we can calculate the -y dB points from the fundamental exactly.

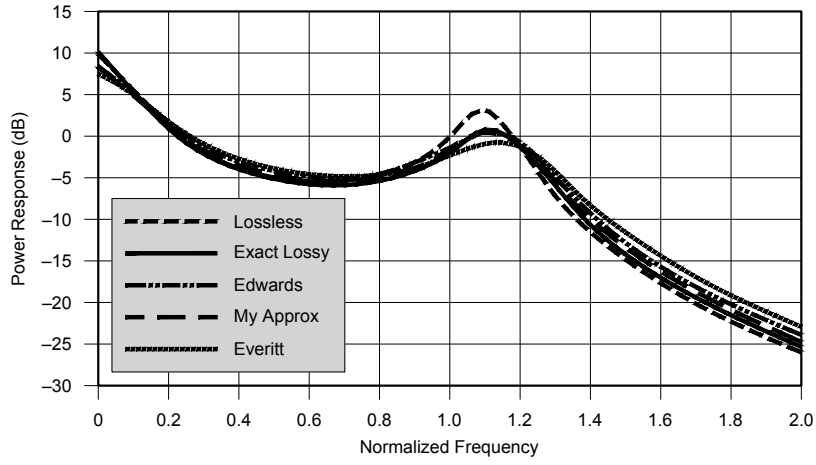

Figure 7 — Universal power response function $G_I(j\omega)$ in dB from Eqn(16) and row 2 of Table 2, for the model parameters given in Table 1 of Part 1. The dashed line is for the lossless model with $Q_1 = 0.942$ and $Q_2 = 4.229$ while the solid curve is the exact lossy model with $Q_1 = 0.872$ and $Q_2 = 5.105$ and $Q_L = 12$. The other curves (dotted and with dot-dashes) belong to the various approximations in Table 1 of Part 1. Note that these functions now peak at a frequency $\omega > 1$ and the concept of a bandwidth at $\omega = 1$ analogous to a conventional resonance circuit is also inappropriate. Nevertheless, we can also calculate the -y dB points from the fundamental exactly (see text).

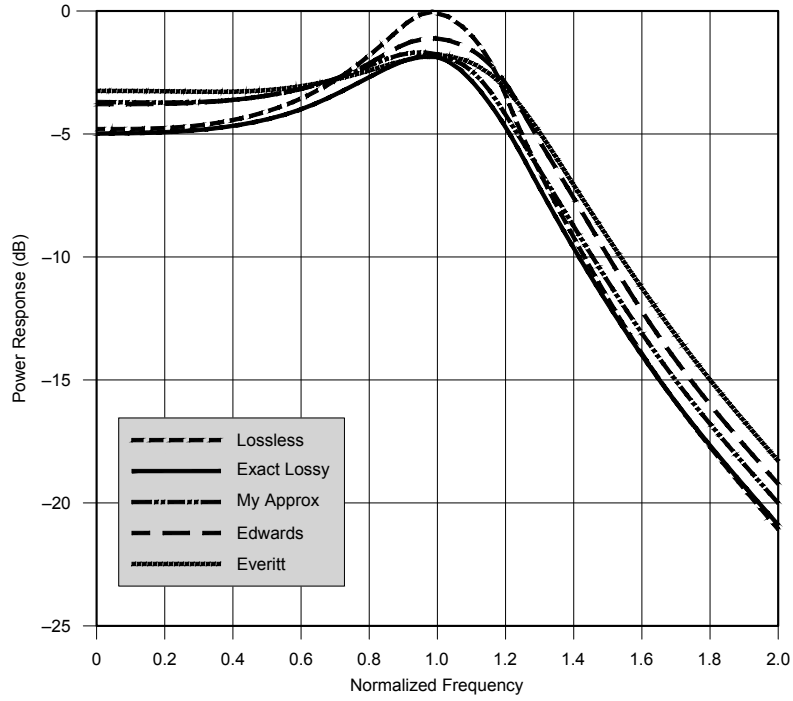

Figure 8 — Universal power response function $G_{term}(j\omega)$ in dB from Eqn(16) and row 3 of Table 2 for the model parameters given in Table 1 of Part 1. The dashed line is for the lossless model with $Q_1 = 0.942$ and $Q_2 = 4.229$ while the solid curve is the exact lossy model with $Q_1 = 0.872$ and $Q_2 = 5.105$ and $Q_L = 12$. The other curves (dotted and dot-dashes) belong to the various approximations in Table 1 of Part 1. Note that the lossless function now peaks exactly at the frequency $\omega = 1$ and the concept of a bandwidth at this frequency analogous to a conventional resonance circuit is thus appropriate. We can in fact now calculate the -y dB bandwidth at the fundamental frequency exactly.

curve (Q_L = 12) as required. From Eqn (16), at dc the value of $G_I(0) = \alpha_G/(a_G)^2$ while at high frequencies $\omega \to \infty$, $G_I(j\omega) \sim \alpha_G/(\omega^3 d_G)^2$ where the coefficients are given by row 2 of Table 2. Note that now the peaks of these curves are at frequencies higher than the design resonance frequency. The exact peak frequency can again be calculated from Eqn (16) if desired by elementary calculus. Also, as we shall see later the exact "bandwidth" can also be calculated, this time by solving a cubic equation.

Finally, in Figure 8 I have plotted $G_{term}(j\omega)$ which a $\omega = 1$ also gives the exact insertion loss of 1.87 dB for the lossy curve (Q_L = 12) as required. From Eqn (16), at dc the value of $G_{term}(0) = \alpha_G/(a_G)^2$ while at high frequencies $\omega \to \infty$, $G_{term}(j\omega) \sim \alpha_G/(\omega^3 d_G)^2$, where the coefficients are given by row 3 of Table 2. Note that now the peak of the lossless response curve is exactly at the design resonance frequency $\omega = 1$, which can be proved by elementary calculus. The exact "bandwidth" can also be calculated by solving a cubic equation, see later.

The reader will note that proper termination is required for the desired harmonic suppression laws: for $G_T(j\omega) = 1/\omega^4$ but for $G_I(j\omega)$ or $G_{term}(j\omega) \sim 1/\omega^6$ as we discussed above. All Pi networks considered here have the characteristics of a low pass filter by design but the pass band characteristics depend very much on the terminations.

5.2. Bandwidth and cut-off frequencies.

We start by calculating the bandwidth for the $G_T(j\omega)$ response function. Let -y be the desired drop in dB from the fundamental frequency response at $\omega = 1$ which is ε in general and we define $x = \varepsilon 10^{-0.1y}$, then from Eqn (16) the upper ω_+ and lower ω_- cut-off frequencies are given by the solution of the quadratic equation inω^2:

$$A\omega^4 + B\omega^2 + C = 0, \tag{21}$$

where the coefficients here are given by:

$$\begin{aligned} A &= \varepsilon^2 Q_U^2 Q_2^2, \\ B &= \varepsilon Q_U Q_2 \left(1+\varepsilon Q_2^2\right) - \frac{1}{2}\left(Q_1+Q_2\right)^2 \\ C &= \left(1+\varepsilon Q_2^2\right)^2 - \frac{\varepsilon}{x}\left(1+Q_1^2\right)\left(1+Q_2^2\right) \end{aligned} \tag{22}$$

It is now straightforward to obtain the upper ω_+ and lower ω_- cut-offfrequencies and in particular the bandwidth $\Delta_T = \omega_+ - \omega_-$. The result from the solution of the quadratic Eqn (21) is:

$$\Delta_T = \sqrt{2}\left[\frac{B}{A} - \sqrt{\frac{C}{A}}\right]^{1/2} . \tag{23}$$

The bandwidth and frequency points for our example Table 1 of Part 1 is tabulated in Table 3. Like the response function, these quantities are all functions of Q_1, Q_2 , and Q_L only. However, it is instructive to examine the L network limit of the bandwidth Eqn (23). For this we shall consider the limit $\varepsilon \to 1$, $Q_1 \to 0$ so the $Q_U = Q_1 + Q_2 = Q_2$. The exact 3.01 dB bandwidth formula from Eqn (23) is now:

$$\Delta_T = \sqrt{2}\left[1 + \frac{1}{2Q_2^2} - \sqrt{1 - \frac{1}{Q_2^4}}\right]^{1/2} . \tag{24}$$

Eqn (24) shows that Q_2 does indeed determine the bandwidth exactly in this case although this is not the standard textbook formula. The latter is only recovered if we take the large Q_2 limit in which case, $\Delta_T = 1/Q_2$, which is our well known *RLC* textbook formula whose voltage response function is:

$$H_{RLC}(j\omega) = \frac{j\omega/Q}{1 - \omega^2 + j\omega/Q} . \tag{25}$$

See for example Hayward[6] and also Eqn (12) of Part 1. From this are easily derived as above the cut-off frequencies and bandwidth formulas for an arbitrary –y dB point or defining $x_y = 10^{-y/10}$:

$$\Delta_T = \frac{1}{Q}\sqrt{\frac{1}{x_y} - 1} , \tag{26}$$

This is in fact the formula used by Reg Edwards, G4FGQ, in his program for calculating bandwidth, see Figures 5 and 6 of Part 1 where he substituted $Q = Q_{Net}$ in Eqn (26). We will see how good Edwards' formula performs later, which is also the essential question posed by Kaune in his first paper[7]. Moving on to the bandwidth for the $G_I(j\omega)$ and $G_{term}(j\omega)$ we have the response functions in Eqn (16) and Table 2. Once again if we define $x = \varepsilon 10^{-y/10}$ then from Eqn (16) the upper ω_+ and lower ω_- frequencies are now given by the solution of the cubic equation in ω^2:

$$d_G^2\omega^6 - 2A\omega^4 + B\omega^2 - C = 0 , \tag{27}$$

where the coefficients are now given in terms of parameters in Table 2 as:

$$\begin{aligned} A &= d_G(c_G + d_G) - (b_G^2/2) \\ B &= (c_G + d_G)^2 - 2a_G b_G \\ C &= (a_G/x) - a_G^2 \end{aligned} . \tag{28}$$

Algebraic formulas for the solution of cubic equations are unduly complicated, although by Descartes' rule of signs[8], for A,

Table 3.

Bandwidth Δ_T for -1 dB and -3 dB points with their upper and lower frequency values. Rows 1 and 2 are calculated exactly using Eqn (23). Rows 3 to 6 are calculated exactly from Eqns (27) and (28) using an online cubic equation solver. These results are also easily checked using the response function equation (16) for example $G_I(j1.227)$ *Lossless* = -3.01 dB. In the last two rows are the approximate results as given by Edwards' program, see Figures 5 and 6 in Part 1. They are obtained from Eqns (25) and (26) using the values of Q_{Net} = 5.17 and 3.61 respectively.

Function	*-1 dB points*	*-3.01 dB points*
$G_T\ (j\omega)$ Lossless	$\omega_+ = 1.0251, \omega_- = 0.7875, \Delta_T = 0.2376$	$\omega_+ = 1.0744, \omega_- = 0.7189, \Delta_T = 0.3555$
$G_T\ (j\omega)$ Exact Lossy	$\omega_+ = 1.0289, \omega_- = 0.7355, \Delta_T = 0.2934$	$\omega_+ = 1.0860, \omega_- = 0.6483, \Delta_T = 0.4377$
$G_I\ (j\omega)$ Lossless	$\omega_+ = 1.1952, \omega_- = 0.9723, \Delta_T = 0.2229$	$\omega_+ = 1.2271, \omega_- = 0.8995, \Delta_T = 0.3276$
$G_I\ (j\omega)$ Exact Lossy	$\omega_+ = 1.2341, \omega_- = 0.9609, \Delta_T = 0.2732$	$\omega_+ = 1.2727, \omega_- = 0.8449, \Delta_T = 0.4278$
$G_{term}(j\omega)$ Lossless	$\omega_+ = 1.1019, \omega_- = 0.8682, \Delta_T = 0.2337$	$\omega_+ = 1.1839, \omega_- = 0.6756, \Delta_T = 0.5083$
$G_{term}(j\omega)$ Exact Lossy	$\omega_+ = 1.1068, \omega_- = 0.7756, \Delta_T = 0.3312$	$\omega_+ = 1.2073, \omega_- = 0.2369, \Delta_T = 0.9704$
$G_{Reg}(j\omega)$ Lossless	$\omega_+ = 1.0504, \omega_- = 0.9520, \Delta_T = 0.0984$	$\omega_+ = 1.1013, \omega_- = 0.9080, \Delta_T = 0.1934$
$G_{Reg}(j\omega)$ Lossy	$\omega_+ = 1.0729, \omega_- = 0.9321, \Delta_T = 0.1408$	$\omega_+ = 1.1479, \omega_- = 0.8712, \Delta_T = 0.2767$

B, C >0 we will be guaranteed either one or three positive roots. Fortunately, nowadays these formulas are now conveniently organized into spreadsheets or as online calculators[9]. Using these tools, I have tabulated the results for the bandwidths in the remaining rows of Table 3. No doubt analytic approximation formulas are available using a variety of methods, see for example Clarke and Hess[10], but I shall not discuss them here.

Suffice to say Table 3 shows that double termination increases the bandwidth in general and that Edwards' estimates in Figures 5 and 6 in Part 1 which are based on Eqns (25) and (26) give rather large errors of more than 50% for the bandwidth in some cases. The estimates for the upper cut-off frequency points are somewhat better with errors of no more than 5% but the lower cut-off frequency points remain quite high over 20%. These results show that the conventional RLC model is a poor approximation in general, even for close proximity to the resonant frequency such as the 1dB cut-off points. Taking into account the factor of 2 in the definition of our results for the bandwidth are consistent with the numerical simulations found in Figure 3 of Kaune [*op. cit.*[7]]. While the bandwidth is in general a function of Q_1, Q_2 and Q_L, it is perhaps instructive to see how poorly Eqn (24) performs as an approximation by comparing it with the results in Table 3. Even in the limit $\varepsilon \to 1$, $Q_L \to 0$ so that $Q_U = Q_1 + Q_2 = Q_2 = Q_{Net}$, Figure 9 shows the percentage errors. This graph illustrates the futility of trying to characterize the Pi network bandwidth in terms of Q_{Net} in general. In the next section we shall examine this question again in the context of harmonic attenuation.

5.3. Harmonic suppression

Given the equations for the power transfer functions, it is straightforward to compute the harmonic attenuation from the various quantities such as $G_T(jn)$, $G_I(jn)$ and $G_{term}(jn)$ for n = 2, 3, 4 respectively, i.e., the second, third and fourth harmonics. These results are tabulated in Table 4 to Table 6. Note that both $G_I(jn)$ and $G_{term}(jn)$ have superior harmonic attenuation than $G_T(jn)$ as expected from the remarks at the end of Section 5.1. Note also that the lossless and Edwards' approximation harmonic figures do not agree with his program outputs, see Figure 5 and 6 in Part 1. Unfortunately, I am unable to trace the origin for these discrepancies. They seem to come from using an approximate semi-empirical *L* network-based formula similar to what I have discussed in Eqn (24). I have found that the following formula, which I shall call the *L* formula:

$$G_R(j\omega) = \frac{1}{Q_{Net}^2\left(\omega^2 - 1\right)^2 + \omega^2} \qquad (29)$$

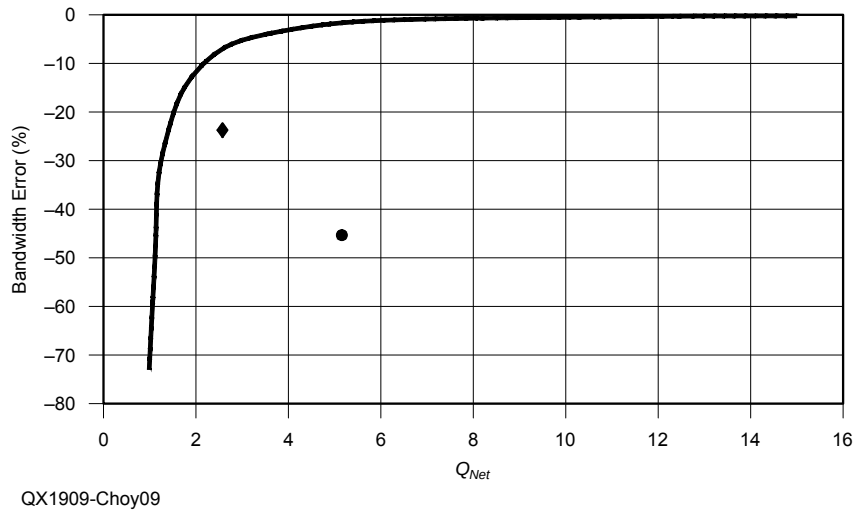

Figure 9 — Bandwidth percentage errors vs. Q_{Net} calculated from Eqn (24) compared with two of the data points from Table 3. The diamond point is for $G_{term}(j\omega)$ and Q_{Net} = 2.585 lossless, and the circled point is for $G_T(j\omega)$ and Q_{Net} = 5.17 lossless.

Table 4.

Harmonic attenuation for the function $G_T(jn)$ calculated using Eqn (16) and the parameters from Table 1 of Part 1.

Harmonic	*Lossless*	*Everitt*	*Edwards*	*My approximation*	*Exact Lossy*
2	15.92	11.63	13.11	12.92	14.13
3	24.35	19.64	21.32	21.11	22.40
4	29.79	24.99	26.73	26.51	27.81

Table 5.

Harmonic attenuation for the function $G_I(jn)$ calculated using Eqn (16) and the parameters from Table 1 of Part 1.

Harmonic	*Lossless*	*Everitt*	*Edwards*	*My approximation*	*Exact Lossy*
2	25.67	20.40	22.33	22.86	23.38
3	38.12	33.08	34.92	35.42	35.94
4	46.19	41.22	43.04	43.53	44.04

Table 6.

Harmonic attenuation for the function $G_{term}(jn)$ calculated using Eqn (16) and the parameters from Table 1 of Part 1.

Harmonic	*Lossless*	*Everitt*	*Edwards*	*My approximation*	*Exact Lossy*
2	21.02	16.50	18.20	18.35	19.04
3	32.66	28.27	29.93	29.98	30.59
4	40.48	36.16	37.80	37.82	38.39

Table 7.

Values for the Lossless and Lossy network calculated using the L formula Eqn (29) compared to the output from Edwards' program, see Figure 5 and 6 of Part 1. None of these values are close to the exact ones calculated for $G_T(jn)$ in Table 4 even though the asymptotic power laws are identical.

n	*Lossless L Formula*	*Lossless Edwards' Program*	*Lossy L Formula*	*Lossy Edwards' Program*
2	23.89	22.7	20.85	21.2
3	32.36	31.6	29.27	30.1
4	37.81	37.2	34.71	35.6

gave values that are quite close to those output by his program, see Table 7. Comparison with Table 4 shows that Edwards must have used a formula that overestimates the harmonic suppression.

6. Comparison with Experiments

Finally, to compare with experiments, we shall take the opportunity to also address the question: what are the effects of a finite Q_L on a predesigned filter which assumed zero inductor loss to start with. For this we will use the formulas in the text and Appendix 2 to compare both the lossless design and the approximate lossy design, i.e., the component values are not adjusted to correct for a finite Q_L and are therefore not the exact values. As most test instruments are based on source and line impedances of 50 Ω, I shall test the theory with experiments for a 50Ω based symmetric Pi network as a preliminary study. Thus, I shall consider the following lossless Pi model with component parameters: L = 1.4 μH, $C_1 = C_2$ = 820 pF, whose design resonance frequency is 5.390811 MHz with a phase lag of 108.48°. The coil was initially made from 17 turns of 0.4 mm enameled wire wound on an Amidon T50-2 (red) core toroid based on Amidon formulas, and the capacitors were 1% polystyrene types. The measured inductance with an LC meter was in fact higher, so two turns were removed, a consequence of the wide spread of A_L values for this mix toroid. The manufacturer's specified unloaded Q for this toroid inductor and frequency is about 230. Accurate measurement for such a high-Q value is not straightforward, the interested reader can refer to excellent articles by Joseph Audet, VE2AZX[11], and Fred Piering, WD9HNU[12], for example. For our purpose it would be useful to estimate its value from the insertion loss given by the response at resonance as measured with a vector network analyzer (VNA). My instrument is a simple Arduino based system driven by an AD9851 DDS synthesizer chip. Measurements are taken for both magnitude and phase through a homemade binocular directional coupler and an AD8302 logarithmic amplifier in transmission mode, see Figure 12. This VNA design has been around for a decade or so in the literature and in its latest incarnation, the

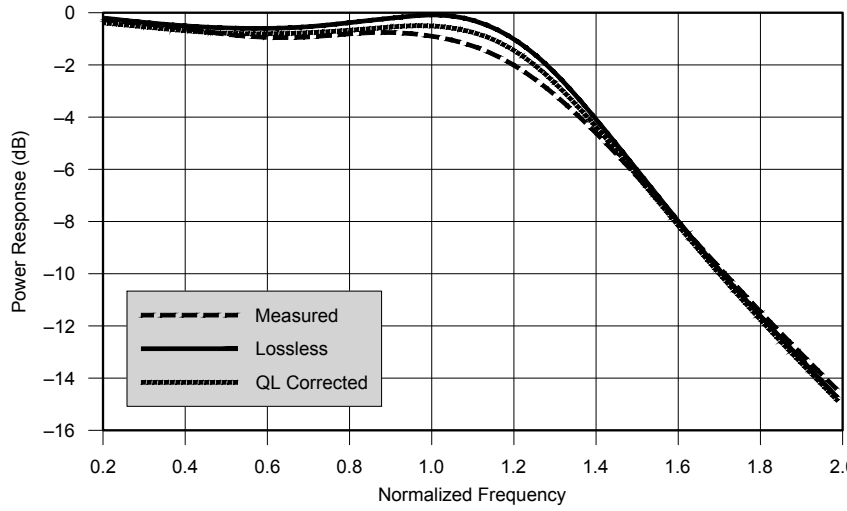

Figure 10 — Power response up to the second harmonic for the symmetric 50-Ω Pi filter design as discussed in the text. The *x* axis is normalized frequency (see Table 8), the *y* axis is the loss in dB. The solid curve plots theoretical Eqn (16) with Table 10 in Appendix 2 for lossless components; the dash curve plots measurements using the F4GOH *VNA*. The data was collected using the DL2SBA *j-VNA* software. The dotted curve applies a finite Q_L value correction to the theoretical lossless curve based on the measured insertion loss of Table 8, see text.

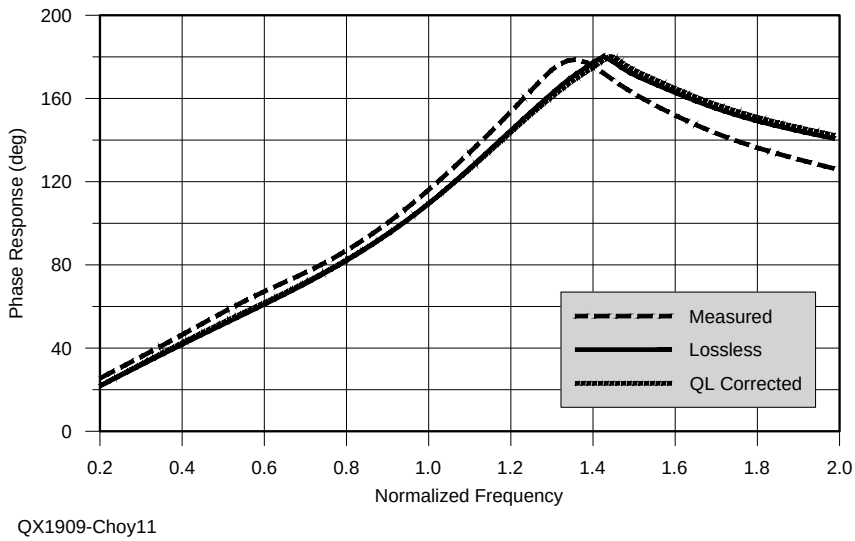

Figure 11 — Plot of the phase angle up to the second harmonic for the symmetric 50 Ω Pi filter design as discussed in the text. The *x* axis is frequency normalized to the theoretical f_0 (see Table 8); the *y* axis is the phase angle in degrees. The solid curve is plotted using the theoretical Eqn (16) with Table 10 in Appendix 2 for lossless components; the dash curve are measurements using the F4GOH *VNA*. The data was collected using the DL2SBA *j-VNA* software. The dotted curve applies a finite Q_L value correction to the theoretical lossless curve based on the measured insertion loss of Table 8, as in Figure 2. Note that the Q_L correction here gives little improvement.

Table 8.

Measured values using the F4GOH's *VNA* and DL2SBA's *j-VNA* software for a symmetric 50 Ω Pi filter design. The component values are L= 1.4 μH, C_1=C_2=820 pF, as given in the text which assumed lossless components. The numbers in bracket are theoretical values for the lossless model. The value for Q_L is an estimate from Eqn (30) of Part 1 based on the measured insertion loss.

f_0 = 5.477 (5.391) MHz	f(-3dB) = 6.893 (7.257) MHz	Insertion loss=0.82dB
Phase angle = 118.4°(108.5)°	R_s=49.3 (50) Ω, X_s=15.9 (0) Ω	Q_L=29.4 (estimated)
2nd f_0 loss = 14.25(14.9) dB	3rd f_0 loss=24.22; (26.84) dB	4th f_0 loss=31.61; (34.79) dB

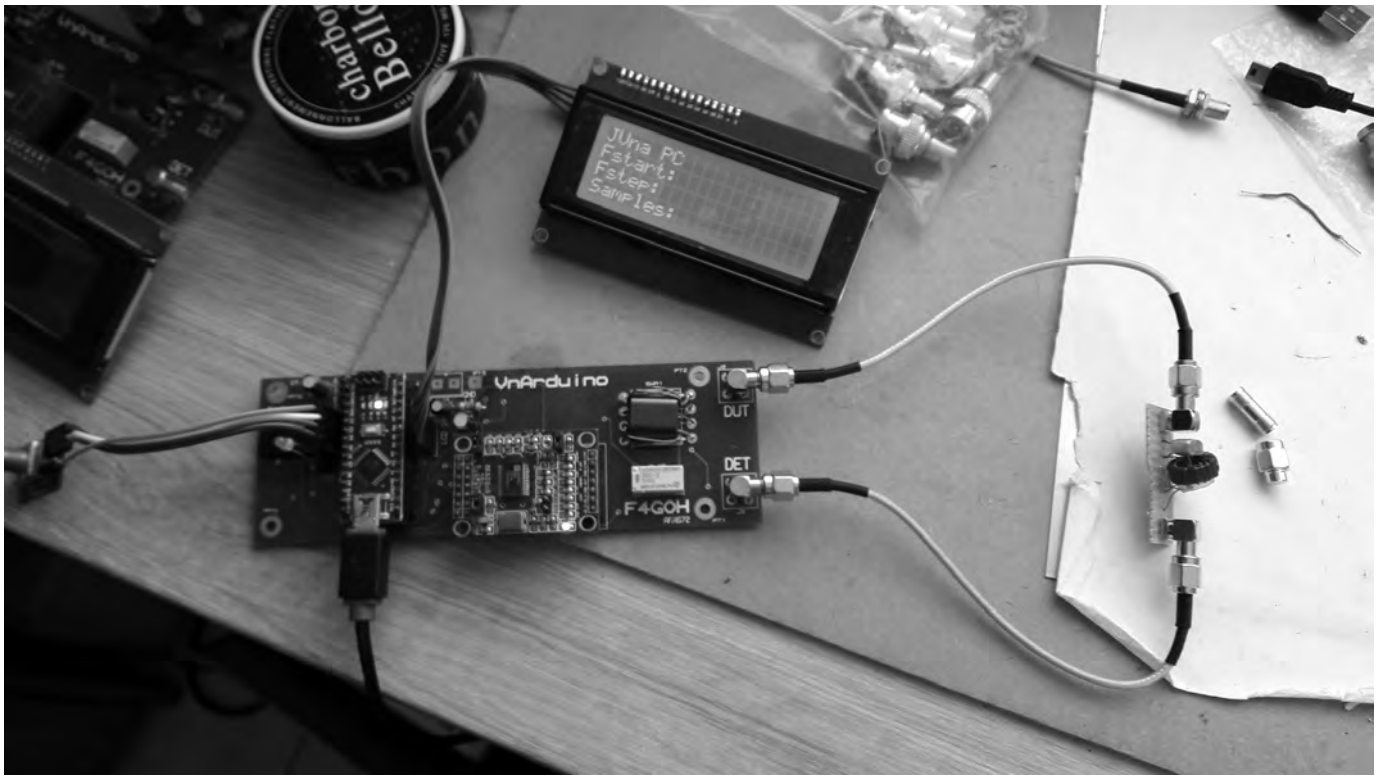

Figure 12 — Experimental set up for measuring the Pi network response with the VNA System designed by F4GOH.

controller is an Arduino nano board, due to Anthony Le Cren, F4GOH[13], which uses the Dietmar Krause,DL2SBA's *java* based *J-vna* software, see Figure 12. I have upgraded it with the suggested SG3386 buffer driver chip which gives an improved dynamic range of 40 dBm. In Table 8 I summarize the measured *vs.* theoretical values for the filter characteristics. In Figure 10, I plot the measured *vs.* design data for the filter. Note that the software enables me to find the measured resonance frequency quite accurately. To do this I terminated one end of the filter with a 50-Ω dummy and switched the scan to reflection mode. From the data the software gives an option to search for a maximum return loss frequency which is given as 5.477 MHz versus the theoretical value of 5.391 MHz with Z_{11} parameters as shown in Table 8. Since the design is lossless $Q_L = \infty$ while the measured values are based on a practical filter with component tolerances and inductor loss, there is an insertion loss and other discrepancies. However, from the insertion loss one can estimate the Q_L value into Eqn (16) and Appendix 2 again, a better result follows as shown by the dotted curve. Finally in Figure 11, is also shown the plot for the theoretical vs. measured phase angles, where surprisingly unlike Figure 10, Q_L corrections show little improvement (a puzzle?). Also, I found that the value of Q_L = 29.4 in Table 8 is substantially below the manufacturer's specifications of the unloaded $Q_L \approx 230$ for this component. To investigate this further, I have used a loosely coupled measurement method with a one turn link from the parallel toroidal coil and capacitor to the VNA in reflection mode [*op. cit.*[11]]. This measurement now gave an unloaded Q_L = 229, a value very close to the Amidon component specs. Readers interested in more accurate measurements on unloaded Q_L of powdered iron toroids can consult the website[14] of John Oppenheimer, KN5L. The studies here imply that in the design equations of Part 1, the coil Q_L to be used should be the loaded value, which will require experimentation under different circuit conditions.

In Conclusion

I hope my two articles will stimulate readers to pay further attention to the synthesis, analysis and comparison with experimental measurements of Pi filters. The analytical method presented here should provide more information than is available from purely numerical simulation software. Further studies of the impedance characteristics will be most interesting. I would like to thank Philip Painter, G3TEX, and Dr. Andrew Smith, G4OEP, for useful comments on the drafts. This paper is dedicated to the memory of Reg Edwards, G4FGQ, and more recently to the late Rev. George Dobbs, G3RJV.

Appendix 1. Some Basic Properties of T Matrices

Proof that the determinant of the T matrix is unity

Let,

$$T = \begin{pmatrix} A & B \\ C & D \end{pmatrix},$$

for the network to be reversible its inverse T^{-1} must exist, so that

$$T^{-1} = \frac{1}{\Delta}\begin{pmatrix} D & -B \\ -C & A \end{pmatrix}$$

where $\Delta = (AD - BC)$ is the determinant.

Since $TT^{-1} = I$ where I is the unit matrix and $\det(T^{-1}) = 1$ therefore $\det(TT^{1}) = \det(T)$ $\det(T^{-1}) = \det(I) = 1$. Thus it follows that $\det(T) = \Delta = 1$; *Q.E.D.*

Determining the ABCD coefficients of the T matrix for an L network.

Referring to Figure 2 for example, a linear network is characterized by the fact that all its components and hence the T matrix coefficients do not depend on input or output voltage or current conditions, although they may depend on frequency. So if we take an open circuit for the output condition, i.e., $I_{out} = 0$, or

Table 9.

Coefficients α_H, a, b, c, and d for $H_x(s)$ in Eqn (14) based on component values.

$x = T$	$\alpha_H = 1, a = 1 + \frac{X_L}{Q_L R_L}, b = \frac{X_L}{R_L} + \frac{X_L}{Q_L \lvert X_{C_2}\rvert}, c = \frac{X_L}{\lvert X_{C_2}\rvert}, d = 0$
$x = I$	$\alpha_H = 1, a = 1, b = \frac{X_L}{Q_L \lvert X_{C_1}\rvert} + \frac{R_L}{\lvert X_{C_1}\rvert} + \frac{R_L}{\lvert X_{C_2}\rvert}, c = \frac{X_L}{\lvert X_{C_1}\rvert} + \frac{X_L R_L}{Q_L \lvert X_{C_1}\rvert \lvert X_{C_2}\rvert}, d = \frac{X_L R_L}{\lvert X_{C_1}\rvert \lvert X_{C_2}\rvert}$
$x = term$	$\alpha_H = 1, a = 1 + \frac{X_L}{Q_L R_L} + \frac{R_S}{R_L}, b = \frac{X_L}{Q_L \lvert X_{C_2}\rvert} + \frac{X_L}{R_L} + \frac{X_L R_S}{Q_L R_L \lvert X_{C_1}\rvert} + \frac{R_S}{\lvert X_{C_1}\rvert} + \frac{R_S}{\lvert X_{C_2}\rvert}, c = \frac{X_L}{\lvert X_{C_2}\rvert} + \frac{R_S}{R_L}\frac{X_L}{\lvert X_{C_1}\rvert} + \frac{X_L R_S}{Q_L \lvert X_{C_1}\rvert \lvert X_{C_2}\rvert}, d = \frac{X_L R_S}{\lvert X_{C_1}\rvert \lvert X_{C_2}\rvert}$

Table 10.

Coefficients α_G, a_G, b_G, c_G, and d_G for $G_x(j\omega)$ in Eqn (16) based on components values. The frequency ω is here normalized to the design frequency ω_0 as usual and as a reminder all reactance values are calculated at this frequency.

$x = T$	$\alpha_G = \frac{R_S}{R_L}, a_G = 1 + \frac{X_L}{Q_L R_L}, b_G = \frac{X_L}{\lvert X_{C_2}\rvert}, c_G = \frac{X_L}{R_L} + \frac{X_L}{Q_L \lvert X_{C_2}\rvert}, d_G = 0$
$x = I$	$\alpha_G = \frac{R_L}{R_S}, a_G = 1, b_G = \frac{X_L}{\lvert X_{C_1}\rvert} + \frac{X_L R_L}{Q_L \lvert X_{C_1}\rvert \lvert X_{C_2}\rvert}\ c_G = \frac{X_L}{Q_L \lvert X_{C_1}\rvert} + \frac{R_L}{\lvert X_{C_1}\rvert} + \frac{R_L}{\lvert X_{C_2}\rvert} - \frac{X_L R_L}{\lvert X_{C_1}\rvert \lvert X_{C_2}\rvert}, d_G = \frac{X_L R_L}{\lvert X_{C_1}\rvert \lvert X_{C_2}\rvert}$
$x = term$	$\alpha_G = \frac{4R_S}{R_L}, a_G = 1 + \frac{X_L}{Q_L R_L} + \frac{R_S}{R_L},\ b_G = \frac{X_L}{\lvert X_{C_2}\rvert} + \frac{R_S}{R_L}\frac{X_L}{\lvert X_{C_1}\rvert} + \frac{X_L R_S}{Q_L \lvert X_{C_1}\rvert \lvert X_{C_2}\rvert}, c_G = \frac{X_L}{Q_L \lvert X_{C_2}\rvert} + \frac{X_L}{R_L} + \frac{X_L R_S}{Q_L R_L \lvert X_{C_1}\rvert} + \frac{R_S}{\lvert X_{C_1}\rvert} + \frac{R_S}{\lvert X_{C_2}\rvert} - \frac{X_L R_S}{\lvert X_{C_1}\rvert \lvert X_{C_2}\rvert}, d_G = \frac{X_L R_S}{\lvert X_{C_1}\rvert \lvert X_{C_2}\rvert}$

$R_L = \infty$, then Eqn (2) gives by simple circuit analysis,

$$V_{out} = \frac{1/y}{Z + 1/y} V_{in} .$$
$$= \frac{1}{1 + ZY} V_{in}$$

Hence the coefficient $A = 1 + ZY$. Since the only current is $I_{in} = YV_{out}$ we have $C = Y$. Now we consider short-circuit output conditions, i.e., $V_{out} = 0$, or $R_L = 0$, then Eqn (2) gives again by simple circuit analysis $I_{out} = V_{in}/Z$ and hence the coefficient $B = Z$ and $D = 1$. Note that the determinant $\Delta = (AD - BC) = 1$ as required, see above and Section 2. In the same way the reader should easily be able to derive the *ABCD* coefficients for the right-handed *L* network as shown in Figure 3.

Appendix 2

This appendix gives the modifications to Table 1 for component-based parameters in Eqn (14) as shown in Table 9. Similarly, the modifications to Table 2 for component-based parameters in Eqn (16) are given by Table 10.

Tuck Choy, MØTCC, received his City and Guilds Amateur Radio certificate in 1971 after high school in Singapore. He then pursued a career in theoretical physics, first as a PhD student and post-doc in London, post-doc at Harwell, then Michigan, assistant professor at Rhode Island and then as a faculty member at Monash University in Australia in 1990. There he took his Morse exams, and took the call sign VK3CCA. His first published homebrew project was a QRP 80 m SSB/CW transceiver using ideas from Gary Breed and Drew Diamond. He won the best technical article award from the Wireless Institute of Australia in 1997. He is now retired but remains active in his professional work and hobbies. Tuck has published a new edition of his book "Effective Medium Theory", Oxford University Press in 2016. He and his wife Debra, who is a professor of linguistics at the Sorbonne in Paris, live in the south of France. In addition to pursuing the foundations of quantum theory, astronomy and ham radio, he has also been an occasional contributor to QEX.

Notes

[1]T. Choy, "On Pi Networks With or Without Inductor Loss - Part 1, Network Synthesis - A Tale of Many Qs." *QEX*, Jul./Aug., 2019, pp. 20-29.

[2]F. Terman, "Fundamental relations existing in four terminal networks," in *Radio Engineer's Handbook*, NY, McGraw-Hill, 1943, pp. 204-215.

[3]M. Valkenberg, "Chapter 13: Two Terminal-Pair Reactive Networks (filters)," in *Network Analysis*, NJ, Prentice-Hall, Inc., 1955, pp. 310-328.

[4]H. Skilling, "Chapter 12 Two Port Networks," in *Electric Networks*, NY, Wiley, 1974, pp. 274-308.

[5]W. Hayward, "Chapter 5 Two Port Networks," in *Introduction to Radio Frequency Design*, ARRL, 1994, pp. 161-172.

[6]W. Hayward, "2.3 - Poles, Zeros and the series tuned circuit," in *Introduction to Radio Frequency Design*, ARRL, 1994, pp. 39-40.

[7]B. Kaune, "Quality Factor, Bandwidth and Harmonic Attenuation of Pi Networks," *QEX*, Sep./Oct., pp. 29-35, 2015.

[8]Wikipedia, **https://en.wikipedia.org/wiki/Descartes%27_rule_of_signs**.

[9]Cubic equation solver, online: **www.1728.org/cubic.htm**.

[10]K. K. Clarke and D. T. Hess, "Parallel resonant transformer-like networks," in *Communication Circuits Analysis and Design*, Reading, MA, Addison-Wesley, 1971, pp. 38-44.

[11]J. Audet, VE2AZX, "Q factor measurements on L-C circuits," *QEX*, Jan./Feb., 2012, pp. 7-10.

[12]F. Piering, WD9HNU, "Building and using an L-Q meter," *QRP Quarterly* (Journal of the QRP Amateur Radio Club International), vol. 55, no. 4, pp. 28-32, 2014.

[13]A. Le Cren, F4GOH, "HF-Arduino VNA," 2015. online: **https://hamprojects.wordpress.com/2016/02/21/hf-arduino-vna-english-version/**.

[14]J. Oppenheimer, KN5L, "Powdered Iron Toroid L-C Q Measurement," online: **https://www.kn5l.net/PowderedIron/**.

Darrel Emerson, AA7FV, G3SYS

4269 N. Soldier Trail, Tucson, AZ 85749; **demerson2718@gmail.com**

Patterns and Polarizations of Modestly-Sized Loop Antennas

Patterns and polarizations of square loops up to about 0.4 wavelengths in perimeter are examined.

In "Small Gap-resonated HF Loop Antenna Fed by a Secondary Loop[1]", K. Siwiak, KE4PT, and R. Quick, W4RQ, provide improved formulas for loop current and impedance, leading to an accurate determination of far-fields and null depths for loops up to 0.3 λ (wavelengths) in circumference. See also, KE4PT and W4RQ, "Small Gap-Resonated HF Loop Antennas[2]". In "Effect of Small HF Loop Near Fields on Direction Finding[3]", KE4PT shows how the near-field response of a small loop can provide polarization at right angles to the normal far field polarization, with the normally expected null in the response being filled in by the near-field response. The combined response can skew the expected loop pattern while direction finding or searching for RFI.

This note investigates some features of the patterns and polarizations in the far field of modestly sized square loops, up to about 0.1 λ on a side.

The expected radiation in the horizontal plane from a very small circular or square vertical loop, as illustrated in many text books, is shown in Figure 1. Figure 1A shows the physical orientation of the vertical loop, and how the horizontal radiation pattern relates to the loop orientation. In the analysis here the square loop is fed in the center of the bottom straight section, and is resonated by a capacitor (not shown) in the center of the top section. Figure 1B shows the far field radiation pattern in the horizontal plane. The pattern was calculated for a very small loop, less than 0.01 λ in size, in free space. In this article any effects of ground are not included. The calculations were performed using *EZNEC Pro*/4[4], which is based on *NEC4*. Details of the feed arrangement are not shown, and any distortions produced by a feeder cable are not included. The radiation peak occurs in the plane of the loop, and is vertically polarized. As expected, there is no significant horizontally polarized radiation, and there is a deep null in the vertically polarized radiation

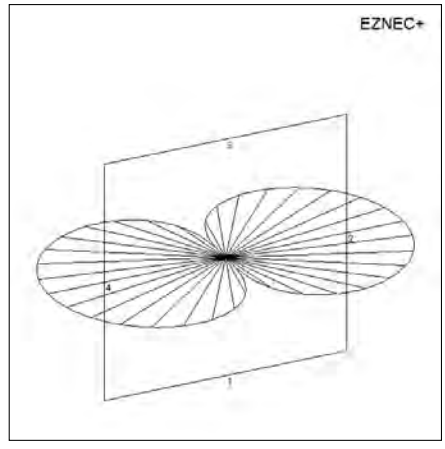

Figure 1A — Orientation of the very small vertical square loop. The loop is fed at the center of the lowest horizontal section (marked "1") with a resonating capacitor at the center of the top horizontal section "3". Radiation pattern is vertically polarized, and with nulls in the broadside directions.

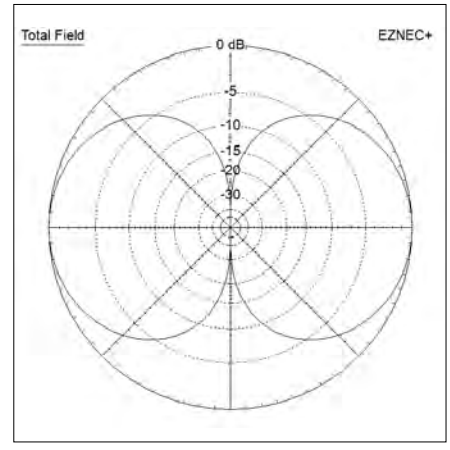

Figure 1B — The far-field radiation pattern of a very small vertical loop, in the horizontal plane. The loop is vertical, in free space, with the plane of the loop running left-to-right. The radiation is vertically polarized, and peaks in the plane of the loop. There is a deep null in the broadside directions.

broadside to the loop.

Figure 2A shows the far-field radiation pattern of a small loop, but where the sides of the loop are now are increased to 0.05 λ, giving a total perimeter of 0.2 λ. This still qualifies as a "small loop", but is beginning to show some of the characteristics of a larger loop. The vertically polarized radiation is shown in the dashed line of Figure 2B, and as expected peaks in the plane of the loop, with a deep vertically polarized null broadside to the loop. There is now some horizontally polarized radiation broadside to the loop, only about 7 dB weaker than the vertically polarized radiation in the plane of the loop. This is shown by the dotted line. The total radiation, a combination of vertical and horizontal polarization, is shown by the solid line at the periphery of the polar diagram. The sharp and deep nulls of the total radiation from the smaller loop, which had been apparent in Figure 1A, are now significantly broadened and relatively shallow.

If used to hunt for RFI, this small loop can give very confusing results. If the source of RFI, even in the far field of the loop, is vertically polarized then only the dashed line in Figure 2B is the relevant polar diagram to use. Using the relatively sharp null in this pattern to identify the RFI, the source of RFI would appear broadside-on to the loop. This is what is normally expected for a small loop. However, if the RFI, still in the far field, happens to be horizontally polarized then the relatively sharp null in the relevant antenna pattern (dotted line) would be found in the plane of the loop, 90° away from the normally expected direction of a null**.** Further, radiation received via the ionosphere has, in general, a continuously changing polarization. For such radiation, no well-defined and stable null in the loop pattern might be discerned at all. This is not a good loop for direction finding.

As the size of a small loop is gradually increased, the relative amplitude of the broadside radiation increases. For a somewhat larger size of 0.1 λ on a side, the resulting far-field radiation pattern is shown in Figures 3A and 3B. A loop of this size barely qualifies as a "small" loop, although still "modest", but the loop now has some very interesting properties.

The vertically polarized radiation is shown by the dashed line in Figure 3B, while the horizontal polarization is shown by the dotted line. The total radiation, a combination of vertical and horizontal polarization, is shown by the solid line. The total power radiation pattern is now nearly omnidirectional in the horizontal plane — within ±0.08 dB in this particular example. With this size of loop the amplitude of horizontally polarized radiation, that peaks broadside to the loop, is almost equal to the vertically polarized radiation in the plane of the loop.

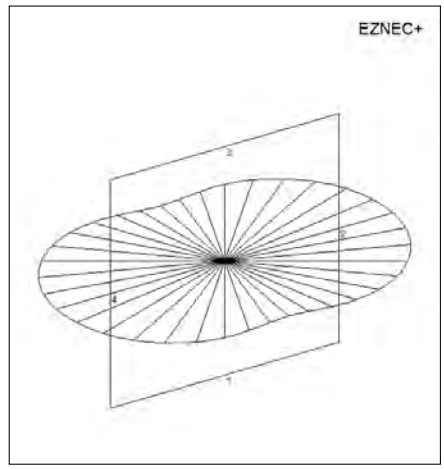

Figure 2A — Far field patterns of a square loop with 0.05 wavelengths sides. The loop is vertical and in free space, fed in the middle of the lower horizontal segment with a resonating capacitor in the middle of the top section.

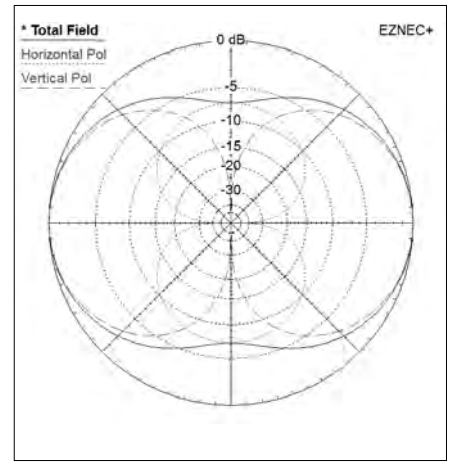

Figure 2B — The horizontally polarized radiation (dotted) broadside to the loop and the vertically polarized radiation (dashed) in the plane of the loop. The nulls in the total field (solid line) are broadside to the loop, now only about 7 dB down on the peak.

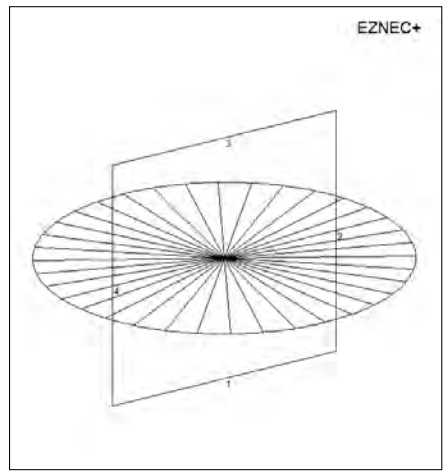

Figure 3A — As in Figure 2, but with the sides of the loop now increased to 0.1 wavelengths. The loop is vertical and fed in the lower, horizontal section, with a resonating capacitor in the center of the top horizontal section. The pattern is shown for the horizontal plane.

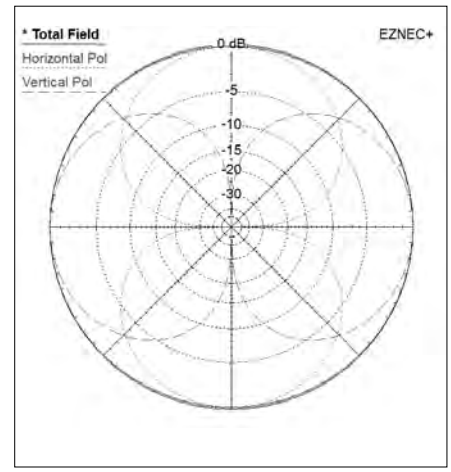

Figure 3B — The horizontally polarized radiation (dotted) broadside to the loop is now very nearly equal to the vertically polarized radiation (dashed) in the plane of the loop. The total radiation (solid) in the horizontal plain is nearly perfectly omni-directional.

Ratio of Horizontal to Vertical Polarization for Small Loops

From Eqn (1) of [*op. cit.*[2]], for a given loop current, the difference between loop current at the top of the loop and current at the bottom of the loop (at the feed point) is proportional to the square of the loop circumference; that is, proportional to the square of the loop diameter. The far field is proportional to this difference in currents, times the effective length of the segments radiating, which is also proportional to the loop diameter. Therefore, for horizontal polarization for a given feed current one would expect the far field to be approximately proportional to the cube of loop diameter. Although that equation applied to a circular loop, one might reasonably expect a comparable expression for a square loop.

For vertical polarization, for small loops the far field is proportional to the length of segment radiating, multiplied by the sine of the phase difference from one side of the loop to the other; the phase difference results from the propagation delay from one side of the loop to the other. For small loops, this sine is

Figure 4 — The ratio of horizontal polarization broadside to the loop compared with vertical polarization in the plane of the loop expected from a small to modest-sized loop. (Note the logarithmic scale used in the horizontal axis for the loop size.) The slope of the dashed line illustrates the expected difference, in dB, based on the very simple discussion in the text. The solid line illustrates the ratio calculated using *EZNEC*, which is not too different from the simple derivation.

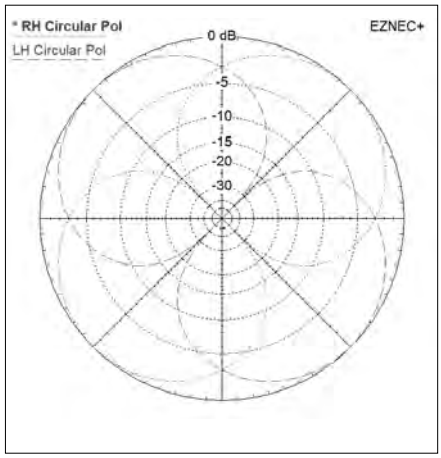

Figure 5 — Far field pattern of the antenna shown in Figure 3, here for circular polarization. The circular polarization can be quite pure. For example, in the top-right quadrant at 45° from the broadside direction the *RH* circular peaks, and the *LH* circular radiation is more than 30 dB down.

approximately proportional to the size of the loop. Therefore for a given loop current one would expect the vertically polarized far field to increase approximately as the square of the loop size. Then for small loops the ratio of horizontally polarized to vertically polarized far field should be approximately proportional to (size cubed)/(size squared), or the ratio of fields should then simply be proportional to the size of the loop. The ratio of radiated powers would be proportional to the square of loop size.

Figure 4 shows the relative strength of broadside horizontal and end-on vertical polarization, calculated using *EZNE*C for square loops of side 0.01 λ up to 0.2 λ. The dashed line illustrates the expected slope of line of the relative ratio if it were indeed just proportional to size of loop, as derived above. The *EZNEC* simulations (solid line with circles) give a slightly stronger dependency on loop size, but given the many approximations inherent in the above simplified discussion, the agreement with the *EZNEC* calculation is fairly good, at least up to loop sides of about 0.1 λ.

Circular Polarization

At an angle 45º away from the plane of the loop, the resultant radiation is a combination of both nearly-equal linear polarizations. Figure 5 shows the same loop as Figure 3, but now the radiation pattern is plotted for left- and right- circular polarization.

At 45º to the plane of the loop, in the upper right quadrant of Figure 5, the *RH* circular radiation (dotted line) peaks. At the same time, the amplitude of the *LH* circular term (dashed line), is more than 30 dB down. At this angle, the circular polarization is very pure. The amplitude at the peak of the *RH* circular varies approximately as cos(θ), where θ is the angle offset from the peak. The amplitude of the *LH* circular term at this point varies approximately as sin(θ). So the ratio of the power in the *LH* circular term compared to that of the *RH* circular term varies as,

$$\frac{LHC}{RHC} = \left[\frac{\sin(\theta)}{\cos(\theta)}\right]^2 .$$

From this equation, the cross-polarized *LHC* term becomes 10 dB below the *RHC* at an angle offset of ±17.5º from the peak *RHC*, for a total effective *CP* beam width of 35º. This is exactly the same result that can be obtained by just comparing the *RHC* and *LHC* powers plotted in Figure 5.

This can be a convenient form of antenna for producing circularly polarized radiation. Apart from the potential use for receiving circularly polarized satellites, this can be a useful HF receive antenna. The received radiation from the ionosphere is often circularly polarized. If both the ordinary and the extraordinary circularly polarized ionospheric rays are being received, then the combination is in general an elliptically polarized wave whose major axis rotates according to the relative phase of the ordinary and extraordinary wave. This rotation (Faraday Rotation) is one of the main causes of fading on HF links. By orientating this loop antenna at 45º to the incoming wave, only one sense of circular polarization can be received, with high rejection of the opposite sense of polarization. This should significantly reduce the fading on

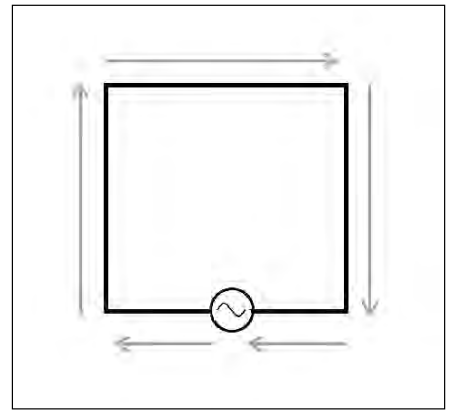

Figure 6 — Square loop fed at the center of the lowest wire, with a tuning capacitor (not shown) at the center of the top wire. The instantaneous phase of current around the loop, as seen broadside on, is very nearly constant. The magnitude of the currents in the left and right vertical sections are equal, although the currents in the two horizontal sections are not. The arrows illustrate the instantaneous direction of current flow.

the signal. Of course, ground reflections will modify the precise sensitivity to different polarizations.

For circular polarization to be generated, there must be a 90º phase difference between the vertical and horizontal components of the radiation. How is that 90º produced in this loop antenna? In a square loop such as this, the current flowing in the two vertical segments of the antenna are equal in magnitude but opposite in direction; see Figure 6. This cancels the vertically polarized radiation broadside to the antenna, but in the plane of the loop, the propagation delay from the left side of the antenna to the right side introduces a phase difference. The fields from the vertical currents, as seen from a far-field distance in the plane of the loop, no longer cancel. So, vertical radiation in the plane of the loop takes place.

Consider the horizontal segments at the top and the bottom of the loop. Because the wires are end-on in the horizontal direction in the plane of the loop there is no radiation from these wires in that direction. The phases of the current in the top and bottom horizontal segments are very nearly equal — the *EZNEC* simulations for the antenna of Figure 3A showed the phases of the currents to be the same within 0.1º. However, Siwiak and Quick [*op. cit.*[1, 2]] showed that the *amplitude* of the currents on the opposite sides of a small circular loop can be significantly different. The *EZNEC* simulation of this antenna showed the current in the top section, opposite the feed point, to be less than half of the current in the bottom section. So, the horizontally polarized radiation from the top and bottom sections of the loop no longer cancel, because

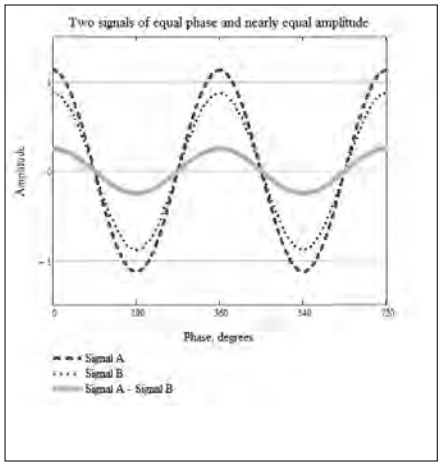

Figure 7A — Signals *A* and *B* represent two cosine waves of equal phase, but slightly different amplitudes. After subtracting the signals, the resultant phase is the same as the phase of the original signals.

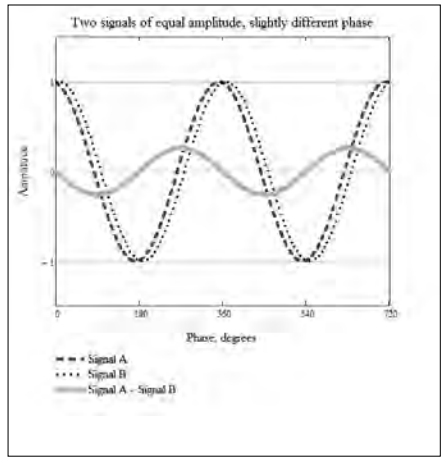

Figure 7B — Signals *A* and *B* represent two cosine waves of equal amplitude, but slightly different phase. After subtracting the signals, the resultant phase is 90º different from the average phase of the original signals.

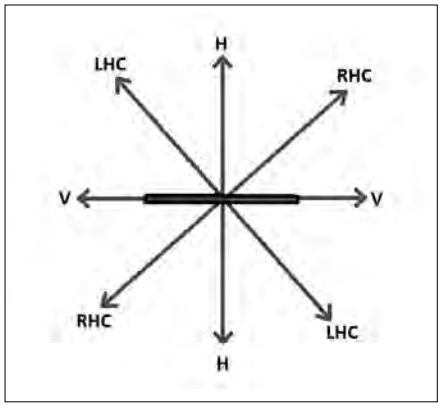

Figure 8 — This loop is sensitive to linear vertical (*V*) or horizontal (*H*) polarization in the plane of the loop or broadside to the loop, or right hand circular (*RHC*) or left hand circular (*LHC*) in the ±45° directions.

of the unequal currents.

For complete cancellation of radiation, the magnitude of the currents in two equal segments must be the same, and their phases must differ by 180º. If there is incomplete cancellation because of unequal magnitude, such as between the top and bottom horizontal sections of the loop, then the phase of the resultant radiation is the same as that of the stronger current. However, if there is incomplete cancellation because of the phases of the current not being 180º different, even though the magnitudes are equal, then the resultant radiation is in quadrature to the mean phase of the original currents. This can be shown easily from the well-known trigonometric relationship for the difference of two cosines. Figure 7B shows graphically how the 90º phase shift appears. For a square loop of side *d*, at a wavelength λ the propagation delay in the plane of the loop causes a phase change of $\pm(d\pi/\lambda)$ radians relative to the mid-point of the loop.

The phase difference between radiation of vertical and horizontal polarization is exactly what is required for the production of elliptically polarized radiation. If the magnitudes of the vertical and horizontal components are equal in a given direction, then the radiation will be 100% circularly polarized. For a square loop of side 0.1 λ, very pure circularly polarized radiation occurs at ±45º to the plane of the loop.

Conclusions

A small loop antenna with its plane vertical is sensitive in the horizontal direction primarily to vertically polarized signals coming from the end-on directions, in the plane of the loop. However, as the loop size in wavelengths increases, there is increasing sensitivity to horizontal polarization from the direction broadside to the loop. For a loop 0.05 λ on a side, or a perimeter of 0.2 λ, this cross-polarized far-field sensitivity is only about 7 dB below the main vertical polarization. In the near field, the situation is more complex. If the loop is used as a directional antenna to search for RFI, depending on the polarization of the transmitted RFI, the measured direction can be as much as 90º in error.

If the loop size is increased to about 0.1 λ on a side, with a perimeter of 0.4 λ, then the sensitivity to horizontal polarization broadside to the loop approximately equals that of vertical polarization end-on to the loop. For reception of signals of arbitrary polarization, the antenna is effectively omnidirectional. At directions ±45º away from the broadside direction, the radiation from the loop becomes circularly polarized, with opposite sense of circular polarization 90º away. Figure 8 illustrates how the loop is sensitive to vertical polarization (*V*) in the plane of the loop, horizontal polarization (*H*) broadside to the loop, or right hand circular (*RHC*) and left hand circular (*LHC*) at the intermediate ±45º directions. Ground reflections still must be considered, but this can prove to be a convenient design of antenna if circular polarization is required, or as a tool to investigate polarization of incoming waves.

Acknowledgement

I wish to thank Jan Hofman, PD2PCH, for many fruitful discussions and experiments with small and moderately sized HF loop antennas.

Darrel Emerson, AA7FV, was first licensed in 1964 as G3SYS, and still holds that call. He obtained a BA in physics from the University of Oxford, and in 1973 a PhD in radio astronomy from the University of Cambridge. His thesis was the first aperture synthesis study of the 21 cm hydrogen emission in the Andromeda galaxy M31. After working for several years at radio astronomy observatories in Germany (becoming DJØOE) and in France (as F6HYR), he came to the USA in 1986 to work for the National Radio Astronomy Observatory as Director of the millimeter-wave observatory at Kitt Peak, AZ. Darrel was part of the design team for the international ALMA radio observatory now in operation in the Atacama Desert in northern Chile, and helped with antenna testing and adjustment during the construction phase. ALMA consists of an interferometric array of 66 precision antennas, observing from 35 to 950 GHz. Darrel retired from NRAO in 2012, and is now a consultant for CORF, a committee which helps to safeguard the frequency spectrum allocated for passive scientific use. He regularly travels to Geneva as a delegate to the ITU. Darrel was very active operating through amateur satellites. He now concentrates on the HF bands using CW and WSPR. Darrel has two sons, Christopher, N7PTE, and Nicholas, KB7OBA. His wife Pam holds the call sign N7UGL.

Notes

[1]K. Siwiak, KE4PT, and R. Quick, W4RQ, "Small Gap-resonated HF Loop Antenna Fed by a Secondary Loop". *QEX* Jul./Aug. 2018, pp.12-17.

[2]K. Siwiak, KE4PT, and R. Quick, W4RQ, "Small Gap-Resonated HF Loop Antennas, *QST* Sep., 2018, pp. 30-33.

[3]K. Siwiak, KE4PT, "Effect of Small HF Loop Near Fields on Direction Finding, Technical Correspondence", *QST* Jul. 2015, pp. 63-64.

[4]Patterns were calculated and plotted in *EZNEC Pro/4* Version 5. Several versions of *EZNEC* antenna modeling software are available from developer Roy Lewallen, W7EL, at **www.eznec.com**.

Kazimierz "Kai" Siwiak, KE4PT

10988 NW 14th St., Coral Springs FL, 33071; **k.siwiak@ieee.org**

Ulrich L. Rohde, N1UL

990 Cape Marco Drive Merida Penthouse 2, Marco Island, FL 34145; **dr.ulrich.l.rohde@gmail.com**

Tuning Short Antennas for Portable Operations

The current sun spots are not favoring HF operation, but there are still enough Amateur Radio applications for low-powered battery-operated radios using whip antennas.

A version of this article appeared in The Microwave Journal, May, vol. 62, ed. 5, 2019.

In general, the whip antenna makes the radio portable, but it is not optimized for signal radiation. A whip antenna has no adequate ground return or proper counterpoise. While some users drag a wire of up to 8 m length behind them[1, 2], this is not always an ideal solution.

This article explores optimizing antenna performance for HF and VHF (1.8 MHz to 54 MHz) portable radios by using an antenna tuning unit (ATU). Among the many available portable transceivers are the Yaesu FT-817/FT-818 (Figure 1A) complemented with an Elecraft T1 automatic ATU (Figure 1B), a Rohde and Schwartz M3TR series SDR transceiver (Figure 2), and the Elecraft KX3 transceiver (Figure 3).

Short Antennas

The first resonant dipole antenna (Figure 4), developed by Heinrich Hertz in 1887, was

▼Figure 1A — The Yaesu FT-817/818 are popular portable transceivers that cover 160 m through 70 cm Amateur Radio bands. [Courtesy of Yaesu]

▶Figure 1B — The Elecraft T1 is an example of a tiny external ATU suitable as an adjunct to the FT-817/818 and other low-power transceivers for portable operation. The T1 also measures SWR and output power. [Courtesy of Elecraft]

Figure 2 — The Rohde & Schwatrz M3TR software defined radio with an internal ATU covers the 160 m through 70 cm Amateur Radio bands. [Courtesy of Rohde & Schwartz]

Figure 3 — The Elecraft KX3 transceiver with an internal ATU is another popular choice for portable 160 m to 6 m operations. [Courtesy of Elecraft]

Figure 4 — In 1887 Heinrich Hertz employed a capacitively loaded dipole driven from a "noisy" spark gap transmitter. [Source: Deutsches Museum in Munich]

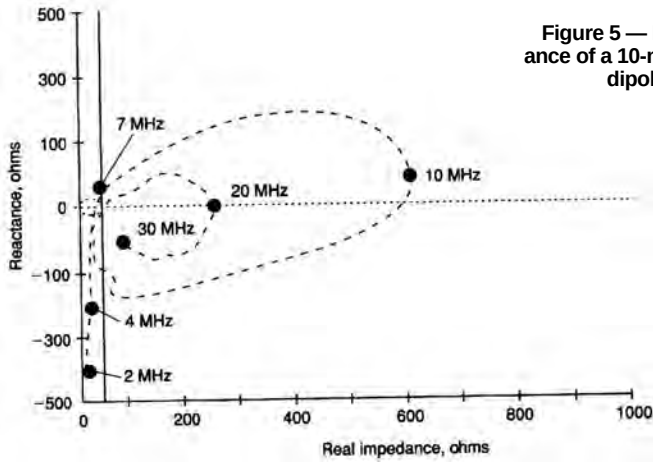

Figure 5 — Measured impedance of a 10-m long symmetrical dipole antenna.

driven from a "noisy" spark gap transmitter. Both dipole legs were equally long and used end-loading metal spheres acting as a capacitive device to reduce the length of the two λ/4 resonant segments.

Now consider a 35-ft long whip antenna, with the feed point connected to a battery operated network analyzer approximately the same size and surface area as a portable transceiver. The analyzer is connected to the antenna with a mechanically small 1:1 ferrite transformer covering 1 to 60 MHz. Figure 5 shows the measured impedance of the whip antenna from 2 to 30 MHz. The typical mobile/portable application using a vertical antenna reflects the evolution of the dipole to a monopole: a symmetrical two-wire antenna made asymmetrical with a transformer and best performing with a set of resonant radials, or a counterpoise, or some kind of grounding.

The magnetic field of the antenna is generated by RF current in the antenna wire or rod and encircles the current in the antenna. The electric field of the antenna is needed for resonance, and joins the antenna tip with its image in the counterpoise (Figure 6). Some antennas are bent into an L shape to make them physically smaller. An example of loading is the capacitive hat, another is a loading coil located about two-thirds of the length (Figure 7) — although this reduces the usable bandwidth.

The electrical equivalent of an electrically short dipole antenna is approximately the series connection of C_A and R_S,

$$C_A = \frac{12.08 \times l}{\log \frac{l}{D}} \tag{1}$$

$$R_F = \frac{Z_a^2 + jR_S.Z_a \tan\left(2\pi \frac{l}{\lambda}\right)}{R_S + jZ_a \tan\left(2\pi \frac{l}{\lambda}\right)} \quad . \tag{2}$$

where C_A, pF, is the equivalent capacitance[3] of the antenna; D, m, is the diameter of the wire; and l, m, is the length of the elements. R_S the radiation resistance; R_F is the impedance of the λ/4 antenna; Z_a is the characteristic impedance of the wire.

Grounding is necessary to close the loop for the currents. Figure 6 illustrates the behavior of the electric field lines for a vertical antenna over ground. Ground loss resistance is depicted by R_t. The field lines penetrate the surface of the earth and produce a current that flows back to the ground point, incurring heat losses. The antenna efficiency η is defined as

$$\eta = \frac{R_S}{R_S + R_v} \tag{3}$$

where R_S is the radiation resistance and R_v is the total effective loss resistance. For elec-

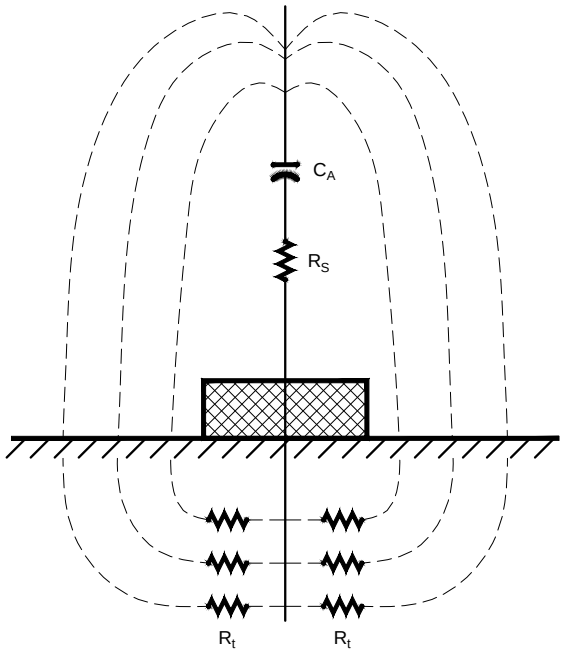

Figure 6 — The electric field of the antenna is needed for resonance, and joins the antenna tip with its image current in the counterpoise.

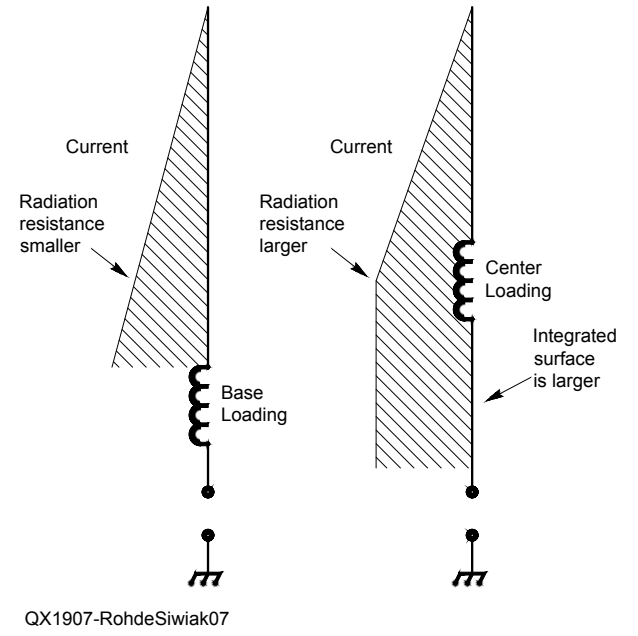

Figure 7 — A loading coil located about two-thirds of the vertical antenna is more effective than a coil at the base.

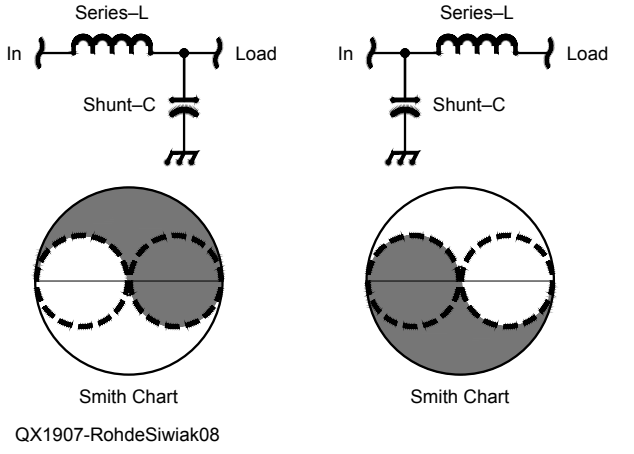

Figure 8 — The reversible L network covers the complementary greyed regions of the Smith chart.

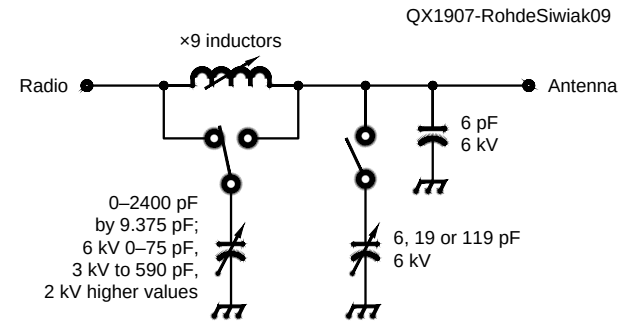

Figure 9 — Simplified schematic of the Icom AH-4 antenna tuning unit. The magic lies in the proprietary algorithms for selecting the match.

trically short antennas with radiation resistance values of only a few ohms, the resulting antenna efficiency can be very low, especially at lower frequencies. In such cases R_v can be reduced with a ground network or a wire network extending over the ground as a counterpoise. All symmetrical antennas, those not excited with respect to ground such as dipoles, benefit from the antenna's independence from the ground resistance — as long as the entire antenna is elevated above the ground.

Radiation Resistance

Electrically short antennas, typically λ/10 or shorter, look like a capacitor with a typical capacitance of 6 pF/m of length for a length-to-diameter ratio of 100, that is, 18 pF for a 3 m rod. At 2 MHz, where the wavelength is 150 m, a 350 μH inductor is required for resonance. The radiation comes from the current in the antenna, not from the voltage. The voltage is maximum at the end. To better understand the radiation, consider the case where the whip antenna length l is λ/4. The vertical radiation pattern of the antenna over ground is[4],

$$F\left(\theta;\frac{l}{\lambda}=\frac{1}{4}\right)=\frac{\cos\left(\frac{\pi}{2}\cos\theta\right)}{\sin\theta} \qquad (4)$$

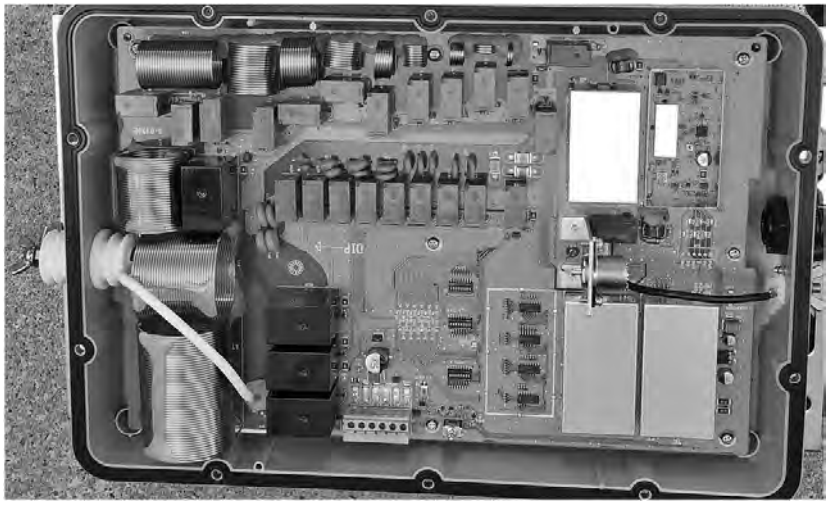

Figure 10 — An internal view of the Icom AH-130 tuner, similar to the AH-4, shows the air-wound coils, capacitors, and switching relays. [Courtesy of Icom]

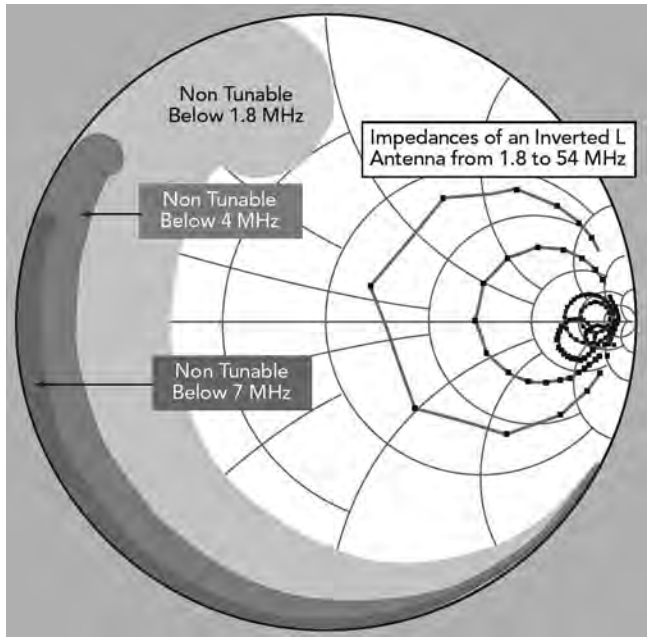

Figure 11 — The tunable ranges of an ATU are frequency dependent. [Source: Microwave Journal]

The radiated power, RF current and radiation resistance of the λ/4 antenna over ground is determined from the power radiated in the half sphere. For the λ/4 antenna,

$$P_s = \tilde{I}_0^2 R_s = \int_{\theta=0}^{\theta=\pi/2} \frac{\overline{E_\theta^2}}{Z_0} 2\pi r^2 \sin\theta d\theta \quad (5)$$
$$= \tilde{I}_0^2 R_s \int_0^{\pi/2} F^2\left(\theta, \frac{l}{\lambda}\right) \sin\theta d\theta$$

so,

$$P_s = \tilde{I}_0^2 R_s \int_0^{\pi/2} \frac{\cos^2\left(\frac{\pi}{2}\cos\theta\right)}{\sin^2\theta} \sin\theta d\theta \quad (6)$$

where,

$$R_s = 60\frac{C + \ln 2\pi - Ci(2\pi)}{4} \quad (7)$$
$$= 60 \times 0.61 = 36.6$$

for the λ/4 antenna. Here $Ci(2\pi)$ = -0.02256, C is Euler's constant (0.577216), and the cosine integral is,

$$Ci(x) = \int_\infty^x \frac{\cos u}{u} du$$

Now, the radiation resistance (*op. cit.*[4]) of the electrically short antenna based on the electric field can be calculated from,

$$P_s = \int_0^{\pi/2} \frac{E_\theta^2}{Z_0} 2\pi r^2 \sin\theta d\theta \quad (8)$$
$$= Z_0\left(\frac{I_0 l}{2\lambda}\right)^2 \cdot 2\pi \int_0^{\pi/2} \sin^3\theta d\theta$$

For the short antenna,

$$R_s = 60\pi^2\left(\frac{l}{\lambda}\right)^2 \int_0^{\pi/2} \sin^3\theta d\theta \quad (9)$$
$$= 40\pi^2\left(\frac{l}{\lambda}\right)^2 = 395\left(\frac{l}{\lambda}\right)^2$$

The radiation resistance of the short antenna is obviously very low.

Effective Height

The open circuit voltage V_o of the antenna is proportional to the antenna field strength E, where the antenna is located,

$$V_o = h_{eff} E \quad (10)$$

The proportionality factor h_{eff} has the dimension of length and is known as the effective height. If the current in the antenna is independent of location (as in a Hertzian dipole), then h_{eff} corresponds to the antenna's geometrical length l. In the general case, h_{eff} is determined by converting the current area into a rectangle with the same area and the maximum current I_0 at its base. Its height is then equal to h_{eff}. Computationally,

$$I_0 h_{eff} = \int_0^h I_y(y) dy, \quad (11)$$
$$h_{eff} = \int_0^h \frac{I_y(y)}{I_0} dy$$

The effective height is related to the effective area A_{eff} and characteristic impedance Z_0 (*op. cit.*[4]) as follows:

$$A_{eff} = \frac{h_{eff}^2}{4}\frac{Z_0}{R_s}; \quad (12)$$
$$h_{eff} = 2\sqrt{A_{eff}\frac{R_s}{Z_0}}$$

For a 35-foot long whip antenna the maximum real impedance is approximately 600 Ω at 10 MHz (λ/2), and the real loss resistance is never below 10 Ω (Figure 5). The imaginary part of the impedance is –400 Ω at 2 MHz.

Antenna Loading and Tuning

Where the whip antenna is inductively loaded affects the antenna's performance. Figure 7 compares base and center loading.

With center loading, both the radiation resistance and integrated surface are larger, which are better for radiation.

The typical low-pass configuration for antenna tuning is a series-L, shunt-C network (Figure 8). In practice, the various components are selected under relay control. For a 35-ft whip antenna operating at 2 MHz, the network needs a series inductor of 100 μH and a shunt capacitor of 262 pF. The tuner needs just two variable elements. Either the left or right capacitor bank in the figure can be selected. The right capacitor bank is used when the load resistance is greater than 50 Ω, and the left capacitor bank is used when the load resistance is less than 50 Ω. In this case at 2 MHz, R = 12 Ω and X_c = −400 Ω, the required series inductor will be 33.42 μH, and the left capacitor bank is used to set a value of 3.18 nF. The most inductive impedance is at 9 MHz, approximately (600 + *j*200) Ω, such that 25 μH and 370 pF are needed for tuning.

The inductance ranges for tuning are found in reversible L network switchable ATUs operating from 1.8 to 54 MHz, where the switched shunt capacitors can be connected to either side of the inductors. Figure 9 shows the matching component ranges of an Icom AH-4 ATU with capacitors on each side of the inductors. In this simplified schematic, the main capacitor bank is switched to either the input or output side of the inductors. The inductors are air-wound with enameled copper wire and have approximately 0.04 μH step size. The capacitor step size is 9.375 pF. This tuner has nine switchable inductors, ten switchable capacitors and two positions for one of the capacitor banks (that is, on either side of the inductors), yielding 1,048,576 discrete tuning combinations.

Table 1

Measured Z=(a+jb) Ω, (L,C) network values, and topology needed for matching with the input transformer set at 1:1 (50 Ω).

Operating Frequency	*a+jb*	*Component values*	*topology*
2 MHz	20 - j540	45 μH, 2000 pF	TX-Cshunt-Lseries-antenna
3 MHz	20 - j400	22 μH, 1300 pF	TX-Cshunt-Lseries-antenna
4 MHz	22 - j294	13 μH, 975 pF	TX-Cshunt-Lseries-antenna
5 MHz	23 - j230	8.1 μH, 609 pF	TX-Cshunt-Lseries-antenna
6 MHz	26 - j186	5.5 μH, 500 pF	TX-Cshunt-Lseries-antenna
7 MHz	26 - j150	4 μH, 440 pF	TX-Cshunt-Lseries-antenna
8 MHz	27 - 118	2.8 μH, 370 pF	TX-Cshunt-Lseries-antenna
9 MHz	33 - j95	2.1 μH, 326 pF	TX-Cshunt-Lseries-antenna
10 MHz	29 - j70	1.5 μH, 270 pF	TX-Cshunt-Lseries-antenna
12 MHz	37 - j14	0.47 μH, 157 pF	TX-Cshunt-Lseries-antenna
14 MHz	145 - j170	0.55 μH, 245 pF	TX-Lseries-Cshunt-antenna
15 MHz	380 - j308	1.8 μH, 115 pF	TX-Lseries-Cshunt-antenna
18 MHz	40 - j118	1.22 μH, 88 pF	TX-Cshunt-Lseries-antenna
21 MHz	40 - j86	0.86 μH, 76 pF	TX-Cshunt-Lseries-antenna
24 MHz	32 - j64	0.33 μH, 99 pF	TX-Cshunt-Lseries-antenna
30 MHz	32 - j40	0.33 μH, 80 pF	TX-Cshunt-Lseries-antenna
50 MHz	41 - j37	0.168 μH, 298 pF	TX-Cshunt-Lseries-antenna

The tuner layout orients the air-wound coils by 90° to minimize coil coupling (see Figure 10). Any number of inductors will not mutually couple if they are placed with their axes forming a 54.74° angle to a common plane,[5] although such placement is not always physically ideal.

Figure 11 graphically depicts the regions on the Smith Chart that can be matched with this ATU. As frequency increases, more of the left-hand side of the Smith Chart is within tuning range of the ATU.

For best performance, antenna tuners use air core coils or very low permeability powdered iron cores. With powdered iron cores, it is possible that some of the measured intermodulation distortion (IMD) products result from ferrite saturation, not from the power amplifier driving the antenna.[6-8]

2 MHz Tuning Example

For a 5 m wire antenna with an 8 m ground wire and a reversible-L network tuner, Table 1 summarizes the antenna impedance and the L and C values needed for matching assuming a 1:1 (50 Ω) input transformer. The LC combination minus the capacitance value of the antenna rod or wire must resonate at the test frequency. Figure 12 shows the antenna resonance tuning configuration and component values at 2 MHz. Figure 13 shows the Re{Z_{11}} and Figure 14 shows the Im{Z_{11}}, both simulated in Ansoft *Harmonica* software. The lower curve in Figure 13 closely matches the desired 20 Ω at

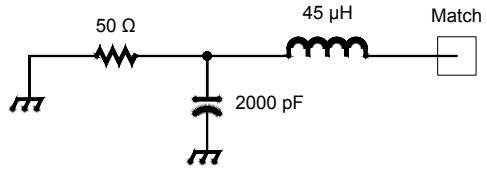

Figure 12 — An L network tuned for 2 MHz. The 50 Ω resistance represents the source impedance.

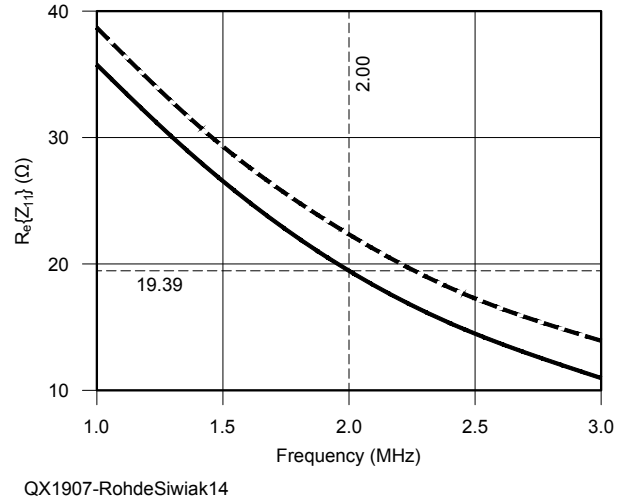

Figure 13 — Simulation of the Re{Z_{11}} with (lower trace) no losses and (upper trace) with a Q of 200.

Table 2

Signal strength measurements 10 m from a Rohde & Schwartz PR100 portable test receiver for the 3 m rod antenna and 10 m long wire dipole in a V configuration. In both cases the dipoles were matched by an ATU.

Frequency	*Signal strength, 3-m rod antenna,*	*Signal strength, 10 m dipole*
3.850 MHz	33 dBμV	46 dBμV
7.185 MHz	31 dBμV	58 dBμV
14.347 MHz	35 dBμV	51 dBμV
18.145 MHz	45 dBμV	60 dBμV
28.400 MHz	76 dBμV	68.7 dBμV

2 MHz, however, it assumes no losses in the tuner. The upper curve assumes a realistic Q of 200, and shows 22 Ω at 2 MHz. Power is I^2R, so a 10% increase in Re{Z_{11}} causes a power loss of approximately 10%; 10 W drops to 9 W available for radiation. These losses are frequently overlooked. While the two-element tuning network produces the desired real and imaginary values, the 8 m ground wire is too short at this frequency, so there is little useful grounding.

Grounding

An antenna tuner can improve the matching, but not the radiation. At a single frequency this asymmetric dipole shows a resonance close to 12 MHz, the antenna-to-case impedance is 37 Ω — almost purely resistive — and the system works. A symmetrical, non-resonant antenna like an inverted V with an elevated tuner and an asymmetrical antenna cable isolating the radio and RF by actually grounding it, will give superior results. If the ATU can tune end-fed, high impedance, low current, long wires, this may be a good solution, although that radio configuration is more of a solution for a stationary setup. A counterpoise is needed for good results.

Table 2 shows signal strength measurements from a 10-m center-fed non-resonant, wire dipole in a V configuration, tuned using an ATU. The measurement is made at 10 m distance using a test receiver with test antenna. For comparison, the table also includes the frequency dependent signal strength for the 3 m rod transmitting antenna.

HF Propagation

We've entered the portion of the 11-year sunspot cycle where communication in the upper HF range has deteriorated. The difference between summer and winter propagation is also a factor. In the summer months beginning in May, the D layer of the ionosphere makes day-time propagation up to 15 MHz difficult; low frequency night propagation works better up to 10 MHz. While propagation forecasts are available on the internet, particularly for long distance connections, the 10 to 600 mile connections are more complex. They are too far apart for VHF/UHF and too close for HF using vertical antennas. The 10 to 600 miles range is best covered using near vertical incidence skywave (NVIS) techniques, employing horizontal dipoles near the ground. Frequencies from 1.8 to 10 MHz would work well, depending on the critical maximum usable frequency. The D layer complicates use of the band. During the day, 5 to 8 MHz provides 300 to 500 mile coverage, which could increase to at least 2000 miles shortly before sunset.

The 20 m Amateur Radio band for voice operation covers 14.150 to 14.350 MHz, but even for this small difference, propagation may vary significantly, as the coherence bandwidth is small.[9, 10]

Many in the Amateur Radio community enjoy low power operation (QRP). Figure 15 shows a Rohde & Schwartz M3TR transceiver, ready for portable ham radio contacts from a boat.

The availability of the range-extending weak signal modes[11, 12] of *WSJT-X*, such as FT8, JT65, and JT9 have made it possible to operate deeper into a darker ionosphere. We

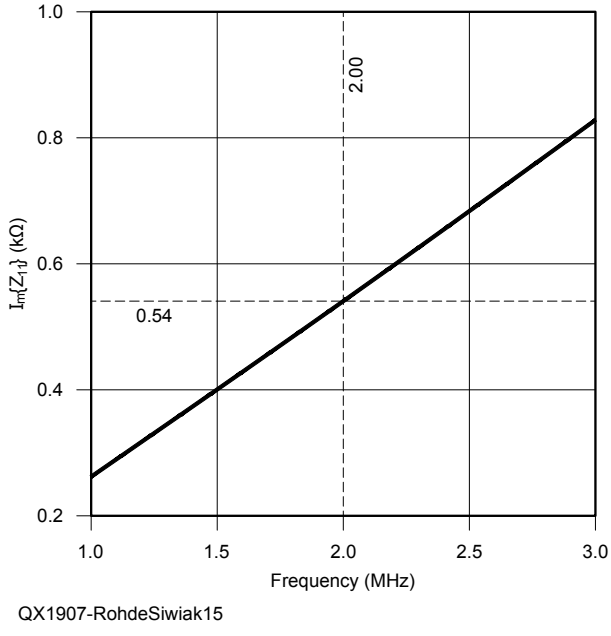

Figure 14 — Simulation of the Im{Z_{11}}.

Figure 15 — Portable installation of a Rohde & Schwartz M3TR transceiver, ready for Amateur Radio contacts from a boat. [N1UL photo]

should also keep in mind that during hurricane season and other natural disasters, using these portable stations helps saves lives.

Summary

For radio communications, the antenna is probably the most critical part of the link, so grounding and antenna tuner losses should be avoided as much as possible. The inductor is always the lossy part of the ATU, while the capacitors are significantly better.

For best operation, antenna radials should be λ/4. One radial is sufficient for tuning, up to four will produce a symmetrical azimuth pattern, and additional radials will reduce ground losses. When λ/4 is not possible, use the longest practical length. Connecting the HF radio ground to a large metallic object is also a good choice. For the tests supporting this article, a grounding spear of about 10 inches, similar to a tent peg, was used.

These requirements for optimum antenna performance make HF portable radios somewhat complicated and difficult, but the link margin equalizing *WSJT-X* modes help tremendously. Well matched and radiating antennas provide the most success. Some of these highly portable radios (Figures 1, 2 and 3) provide vital communications in disaster areas — as demonstrated recently in Puerto Rico and in South Florida.

Prof. Dr.-Ing. habil. Dr. h.c. mult. Ulrich L. Rohde, N1UL, is the Chairman of Synergy Microwave Corp., Paterson, NJ; President of Communications Consulting Corporation, serving as an honorary member of the Senate of the German Joint Forces University Munich; honorary member of the Senate of the Brandenburg University of Technology Cottbus-Senftenberg, Germany; past member of the Board of Directors of Ansoft Corporation, Pittsburgh, PA; and is a partner of Rohde & Schwarz, Munich, Germany. Prior to being appointed Honorary Professor of RF and Microwave Technologies at the University of Cottbus, Dr. Rohde was appointed Visiting Professor of RF and Microwave Technologies in November 2001 at the University of Cottbus, Germany; was member of the staff at George Washington University (1982) and as an adjunct professor at the University of Florida, Gainesville, teaching in the Electrical Engineering and Computer Sciences departments. He presented numerous lectures worldwide regarding communications theory and digital frequency synthesizers. He is also a full professor at the University of Oradea. Dr. Rohde has published more than 300 scientific papers in professional journals and several books and book chapters, and several dozen patents. Dr. Rohde is a Fellow Member of the IEEE, Member of the IEEE Technical Committee for HF, VHF, and UHF Technology MTT- 17, Member of the IEEE Signal Generation and Frequency Conversion MTT-22, Member of the Board of Trustees Fraunhofer Gesellchaft (EMFT) for Modular Solid State Technology, Member of the Board of Friends of the Bavarian Academy of Science and Humanity, and Honorary Member of the Academy of Science, all in Munich, Eta Kappa Nu Honor Society, Executive Association of the Graduate School of Business Columbia University, NY, the Armed Forces Communications & Electronics Association, Fellow of the Radio Club of America, former Chairman of the Electrical and Computer Engineering Advisory Board at New Jersey Institute of Technology, IFCS C. B. Sawyer Award recipient, IFCS I. I. Rabi Award recipient, Honorary Professor at IIT Delhi, India, Chief Judge of IEEE IMS 2014 Student Design Competition, and PhD Defense Committee Member at UCLA and Drexel University. His hobbies include sailing, US Merchant Marine Officer, Master of Steam or Motor Vessels, photography and licensed Amateur Radio operating since 1956 (DJ2LR and N1UL).

Kazimierz (Kai) Siwiak, KE4PT, holds an Amateur Extra class license. He earned his PhD from Florida Atlantic University, Boca Raton, FL, specializing in antennas and propagation, and earned the BSEE and MSEE degrees from the Polytechnic Institute of Brooklyn, Brooklyn, NY (now New York University Tandon School of Engineering). He is a registered Professional Engineer in Florida and Life Senior Member of IEEE. Dr. Siwiak holds 41 US patents, has authored many peer-reviewed papers, several textbooks, and has contributed chapters to other books. Kai is a life member of AMSAT, and member of ARRL where he serves on the RF Safety Committee and as Technical Advisor. He is a QST Contributing Editor, and Editor of QEX. Kai is a dedicated DXer and enjoys portable operating. In 2014 he operated as ZL/KE4PT from portable locations around Wellington, New Zealand. His interests include flying (instrument and multi-engine commercial pilot), hiking, and camping.

Notes

[1]U. L. Rohde, 'Die Anpassung von kurzen Stabantennen fur KW-Sender", Funkschau 1974, heft 7.

[2]K. Siwiak, "*Ionospherica* – How Dipoles Radiate — The Hiker's Bent Dipole", *QRP Quarterly*, Spring 2014.

[3]K. T. McDonald, "Reactance of Small Antennas", Joseph Henry Laboratories, Princeton University, Princeton, NJ, (updated Feb. 8, 2018) online: **puhep1.princeton.edu/~mcdonald/examples/cap_antenna.pdf**.

[4]E.C. Jordan and K.G Balmain, **Electromagnetic Waves and Radiating Systems, Second Edition**, Prentiss-Hall, NJ, 1964.

[5]K. Siwiak and Y. Bahreini, **Radiowave Propagation and Antennas for Personal Communications, Third Edition**, 2007, Artech House, Norwood, MA, pp. 20-22.

[6]U. L. Rohde, "Theory of Intermodulation and Reciprocal Mixing: Practice, Definitions and Measurements in Devices and Systems, Part 1, *QEX*, Nov./Dec. 2002, pp. 3-15.

[7]U. L. Rohde, "Theory of Intermodulation and Reciprocal Mixing: Practice, Definitions and Measurements in Devices and Systems, Part 2, *QEX*, Jan./Feb. 2003, pp. 21-31.

[8]"The ARRL Handbook for Radio Communications, 2019 Edition," Section 21: Antennas. Available from your ARRL dealer or the ARRL Bookstore, ARRL item no. 0888. Telephone 860-594-0355, or toll-free in the US 888-277-5289; **www.arrl.org/shop**; **pubsales@arrl.org**.

[9]U. L. Rohde, J. C. Whitaker, H. Zahnd, **Communications Receivers: Principles and Design", 4th Edition**, McGraw Hill, 2017.

[10]**https://synergymwave.com/articles/2016/Antenna_presentation.pdf**.

[11]J. Taylor, S. Franke, and W. Somerville, "Work the World with *WSJT-X*, Part 1: Operating Capabilities", *QST*, Oct. 2017, pp. 30-36.

[12]J. Taylor, S. Franke, and W. Somerville, "Work the World with *WSJT-X*, Part 2: Codes, Modes, and Cooperative Software", *QST*, Nov. 2017, pp. 34-39.

Maynard A. Wright, W6PAP

6930 Enright Dr., Citrus Heights, CA 95621; **m-wright@eskimo.com.**

More *Octave* For Complex Characteristic Impedance

The author considers transmission lines with characteristic impedance angle near minus 45 degrees.

In a previous article[1], we explored what happens when the characteristic impedance of a transmission line Z_0 is complex, rather than real. We found that, in most cases of interest to Amateur Radio, real Z_0 is a reasonable assumption or approximation. In some cases though, the imaginary part of Z_0 might make a significant difference in calculated and/or measured results.

One case we considered involves Z_0 with an angle at or near -45°. This case closely approximates the behavior of telephone cable pairs or other transmission lines at voice frequencies. When a transmission line with such a Z_0 is terminated in a conjugate impedance, the reflection coefficient and VSWR are both large, but the amount of power consumed in the load impedance is more than for any other termination. This seems counter intuitive, so we'll look at it a bit more. Examination of such an extreme case will help with all the mismatches that involve complex Z_0, but the extreme case makes certain facts stand out so as to shed light on the matter.

First, we'll examine the same transmission line that we used to produce Figures 1 and 2 in the previous article. We'll use the code from Table 3 — available on the **www.arrl.org/QEXfiles** for (*op. cit.*[1]) — but we'll terminate it in Z_0 to produce Figure 1 in this article and in the conjugate of Z_0 to produce Figure 2 here. To avoid dividing by zero — where the VSWR becomes infinite — we will use $Z_L = 50 + j49.999$ and $Z_0 = 50 - j49.998$ rather than$(50 + j50)$ and $(50 - j50)$ in our *GNU Octave* code.

We will need to increase the resolution of the abscissa ("distance along line" axis) to properly capture the sharp negative excursions of the VSWR curve for the conjugate termination case. To accomplish this, we changed the number of elements in array *z* from 200 to 2000. The modified code is listed here in Table 1.

Note that there is no reflected wave, and therefore no standing wave in Figure 1. In Figure 2 the standing wave is significant. The limits of the envelope reach from 0 to 2 V at the load. So there is a significant reflection from the load for the conjugate termination, and no reflection at all for the image (matched) termination.

Looking at this seemingly odd situation, we'll take advantage of the fact that energy in any circuit is transferred by means of the electromagnetic field that travels among various circuit elements. Even for a dc circuit, such as a battery and a light bulb, the behavior of the circuit may be analyzed either by considering the electromagnetic field traveling along the wire pair or by considering the voltage and currents in the circuit. Individual electrons move only short distances in a conductor before recombination, so the flow of current is one of large scale migration and the energy itself is carried in the fields generated by the massive number of very short dashes of electrons[2, 3]. Electromagnetic waves can flow in either direction in such a circuit just as they do in a transmission line. Using that equivalence, we'll analyze a circuit of lumped components that represents the conjugate impedance match and extrapolate the results to our situation with the transmission line.

The circuit is shown in Figure 3. We'll let the phase of V_S be the reference for the circuit. Since the positive and negative reactances cancel each other in the series circuit, the impedance seen by V_S will be 100 Ω real and the current flowing in the circuit will then be 0.02 A, real. V_S along with impedance Z_0 may represent the voltage and impedance seen looking back from the load into a transmission line of any length.

We'll use a technique described by Everitt and Anner[4] to split the load impedance of Figure 3 into two segments, one provides an image impedance and the other adds to that image impedance to produce the original conjugate load. We show this circuit in Figure 4. Externally, the load looks exactly the same electrically as does the load in Figure 3.

A simplified form of the compensation theorem[5] states that "any impedance in a network (either linear or nonlinear) may be replaced by a generator of zero internal impedance, whose generated voltage at every instant is equal to the instantaneous potential

Table 1.

***Octave* code.**

```
graphics_toolkit gnuplot;
gamma = 0.01 + 1j * 0.5; # Used to generate Figure 2
Zo = 10 - 1j * 10;
# Zl = Zo;        # Used to generate Figure 1
Zl = 10 + 1j * 10; # Used to generate Figure 2
rho = (Zl - Zo) / (Zl + Zo);
V1 = 1.0;
p = log(1 / sqrt(abs(rho)));
q = -0.5 * arg(rho);
l = 16 * pi;
z = linspace(0, l, 2000);
d = l .- z;
Vdabs = sqrt((sinh(real(gamma) .* d .+ p)) .^ 2 + (cos(imag(gamma) .* d .+ q)) .^ 2);
  # (8.17)
scale_factor = abs(2 .* V1 * e .^ (-1j .* imag(gamma) .* l) .* sqrt(rho));
Vdabs = scale_factor .* Vdabs;
upper_bound = scale_factor .* cosh(real(gamma) .* d .+ p);
lower_bound = scale_factor .* sinh(real(gamma) .* d .+ p);
upr_bnd = upper_bound(2000);
lwr_bnd = lower_bound(2000);
plot(d, Vdabs, d, upper_bound, d, lower_bound);
grid();
xlabel("DISTANCE ALONG LINE => TOWARD TRANSMITTER");
ylabel("LINE VOLTAGE: ABSOLUTE VALUE");
pause;
```

difference produced across the replaced impedance by the current flowing through it." We'll use this theorem to replace Z_{L2} in Figure 4 with V_R in Figure 5. The voltage generated by V_R is,

$$V_R = I \cdot Z_{L2} = 0.02 \cdot j100 = +j2.0 \text{ V} \quad (1)$$

We now have a circuit with two voltage sources, one of which, V_S, is responsible for both providing a matched reflection-free signal to Z_{L1}, and for producing reflected voltage V_R.

Using superposition, we can calculate the currents that will be caused to flow in the circuit by each voltage source, V_S and V_R, independently and then add them algebraically to determine the total current flow. I_1 current due to V_S is,

$$\begin{aligned} I_1 &= V_S / (Z_0 + Z_{L1}) \\ &= 2.0 / \left[(50 - j50) + (50 + j50) \right] \\ &= (0.01 + j0.01) \text{ A} \end{aligned} \quad (2)$$

and I_2 current due to V_R is,

$$\begin{aligned} I_2 &= V_R / (Z_0 + Z_{L1}) \\ &= j2.0 / \left[(50 - j50) + (50 - j50) \right] \\ &= (-0.01 + j0.01) \text{ A} \end{aligned} \quad (3)$$

Since the positive senses of the sources are oriented away from each other, as shown in Figure 5, the two currents, as specified, are flowing in opposite directions. The total current, therefore, is found by subtracting I_2 from I_1,

$$I = I_1 - I_2 = 0.02 \text{ A} \quad (4)$$

This agrees with our original calculation of the current. Using Figure 5 we'll calculate the voltage at the load from each source as follows,

$$\begin{aligned} V_{L1} &= V_S \cdot Z_{L1} / (Z_0 + Z_{L1}) \\ &= 2.0 \cdot (50 - j50) / \left[(50 - j50) + (50 - j50) \right] \\ &= 1 \text{ V} \end{aligned} \quad (5)$$

and

$$\begin{aligned} V_{L2} &= V_R \cdot Z_{L1} / (Z_0 + Z_{L1}) \\ &= j2.0 \cdot (50 - j50) / \left[(50 - j50) + (50 - j50) \right] \\ &= j1 \text{ V} \end{aligned} \quad (6)$$

V_{L1} results from the current due to the incoming (incident) electromagnetic wave and V_{L2} produces a reflected electromagnetic wave that travels back toward the source.

The two voltages combine as $(1 + j1)$ V, which matches what we calculated earlier. Now we'll imagine that we can back up along the transmission line represented by the components inside the dashed lines of Figures 3, 4 and 5. We'll assume that the transmission line is lossless. The angles of the vector volt-

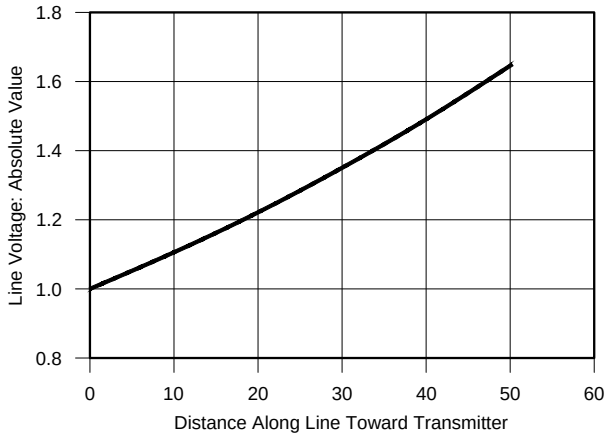

Figure 1 — Voltage along line away from image impedance termination.

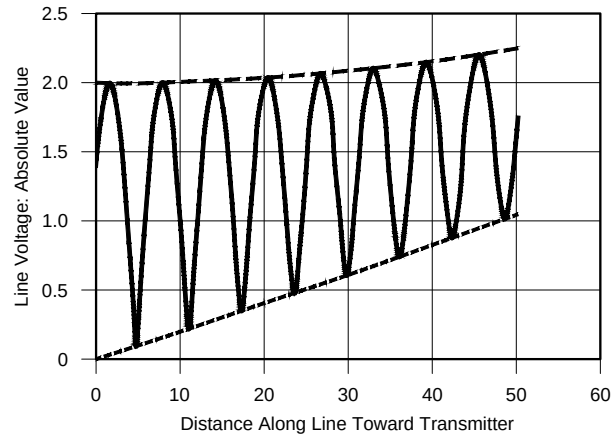

Figure 2 — Voltage along line away from conjugate impedance termination.

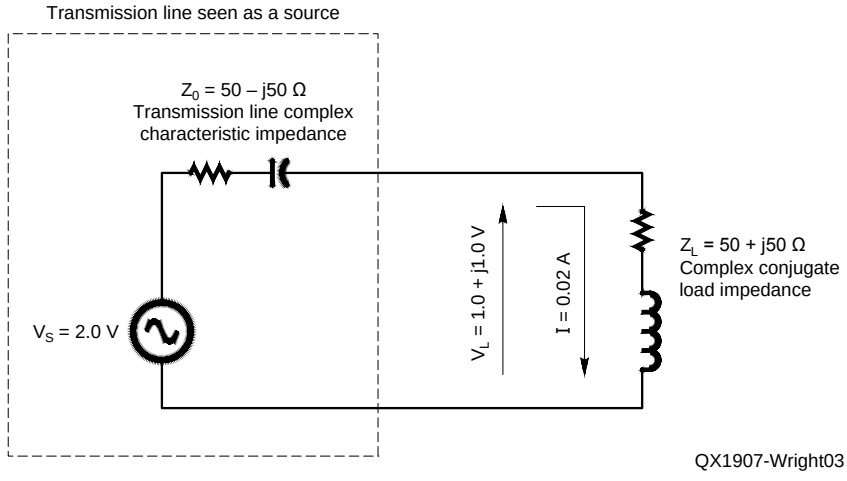

Figure 3 — Conjugate termination shown normally.

ages V_{L1} and V_{L2} will rotate in opposite directions as we back up along the line, coming in and out of phase alternately at 90° intervals. Ignoring the effects of attenuation, when the two voltages are in phase, they reinforce to produce 2 V. When they are out of phase, they cancel to 0 V.

This is what we see in Figure 2, where the envelope of the voltages along the line reaches from 0 to 2 V. The VSWR will be 2 divided by 0, yielding the infinite VSWR that we see in the calculations. Although we concluded in the previous article that a complex Z_0 would cause errors in the calculation of VSWR, it appears that we have now shown that the traditional calculations of reflection coefficient and VSWR are not in error in this extreme case. It's apparent, though, that they will not be useful in predicting line loss accurately using the usual calculations or graphical methods.

Note that in the case of a transmission line that is short-circuited or open-circuited, the reflection coefficient is either +1 or -1, real value in either case, indicating that all the power is being reflected from the end of the line. In our case the reflection coefficient is $+j1$. All three terminations — shorted, open, and conjugate — yield reflection coefficients that have a magnitude of 1. Since the angle of the reflection coefficient is discarded in the calculation of VSWR, the VSWR will be exactly the same: infinite, for each case.

Chipman[6] states that the reduced loss in the case of the conjugate match is caused by combining of the incident and reflected waves in the section of line near the load. For a conjugate match, the phase relationships of the two waves yield less loss in the line than is the case for an image impedance match. Chipman notes that this effect occurs in a relatively short section of the transmission line close to the load because the loss per wavelength associated with a large angle Z_0 is necessarily high because of the relationships among the primary constants that lead to the non-real Z_0.

For certain combinations of Z_0 and Z_L, the reflection coefficient can exceed a magnitude of 1 and can be as high as 2.41 (*op. cit.*[6]). This is not a violation of the law of conservation of energy because the energy constituting the reflected wave is obtained from energy that was initially received from the incident wave and stored in the reactive element(s) of Z_L. This situation reminds us of resonance, where the voltages across various circuit elements may exceed the voltage supplied to the circuit.

Although Everitt and Anner provide a method for solving for impedances and losses, including complex Z_0, using a step-by-step procedure[7] it is easier today to build a T-equivalent network[8] or ABCD matrix (*op. cit.*[1]) using software such as *GNU Octave* and to use such models to calculate losses and impedances as desired. We might also use *TLW*, a versatile transmission line analysis program packaged with *The ARRL Antenna Book*[9]. These methods are completely general and can handle either real or complex characteristic impedances equally well.

An expression for "loss due to SWR" — the additional loss over matched-line loss that is caused by a mismatch — was contributed by Charles Michaels, W7XC, in 1997[10]. His expression requires the impedance of the load Z_0 and the impedance at another location back toward the originating end of the line but it doesn't require the reflection coefficient

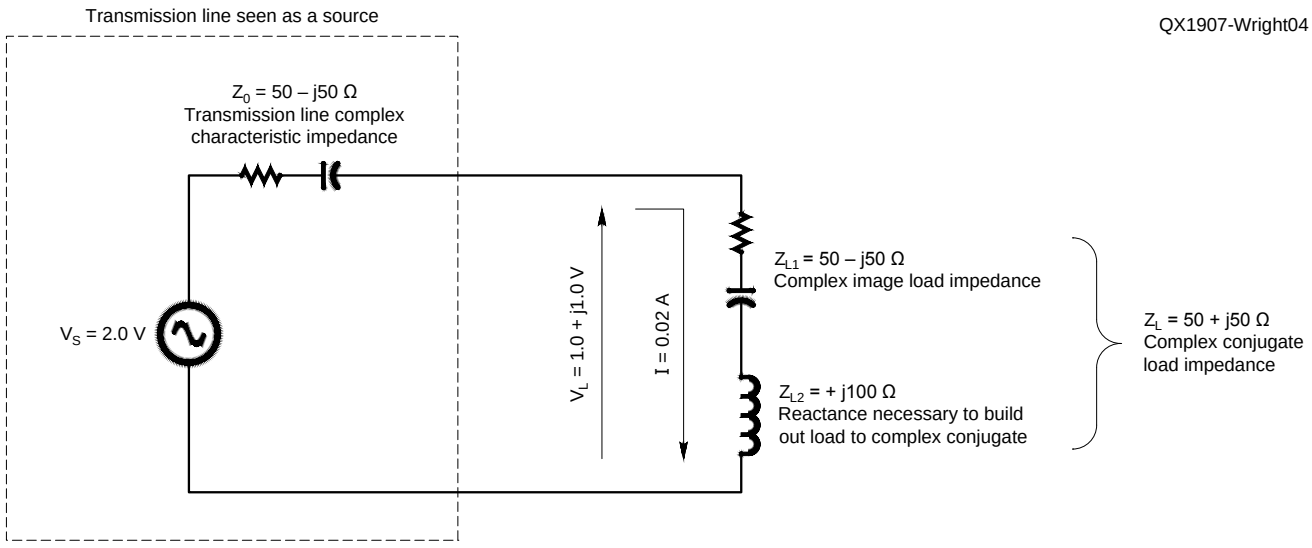

Figure 4 — Conjugate termination shown split.

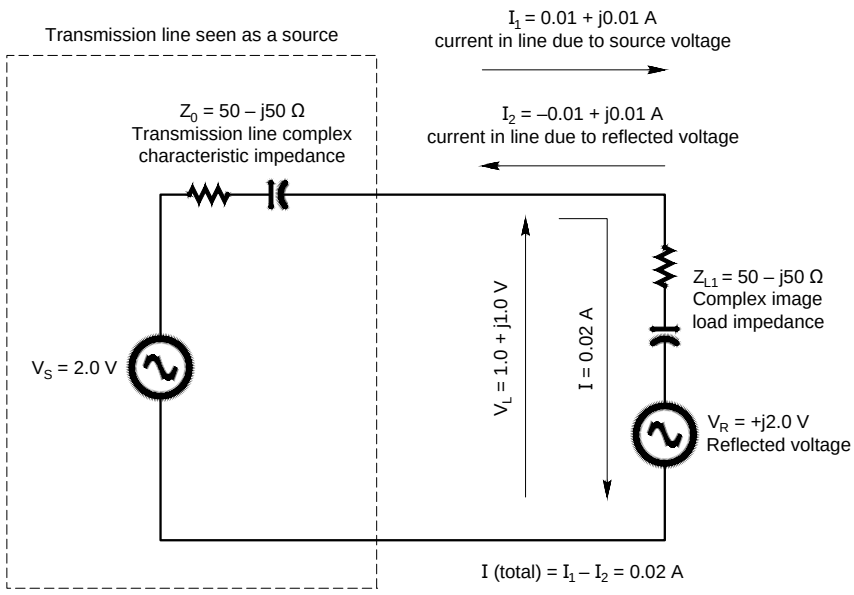

Figure 5 — Conjugate termination with V_R replacing +j100.

Table 2.

***Octave* code**

```
Zo = 50 - 1j * 16;              # transmission line characteristic impedance
ZL = 200 - 1j * 190;            # load impedance
Zl = 63.147 - 1j * 47.085;      # impedance at a point on the line back toward the source
Added_loss = 10 * log10((1 - (abs((Zl - conj(Zo)) / (Zl + Zo))) ^ 2) /
   (1 - (abs((ZL - conj(Zo)) / (ZL +Zo))) ^ 2))
```

or VSWR. Charles' expression is accurate and useful for lines with real or complex Z_0, but it does require the measurement or calculation of the complex impedance of the line at two points as inputs to his equation. *GNU Octave* code that implements Charles' equation is listed here in Table 2. Omission of a terminating semicolon in the expression for the variable "Added_loss" will cause the value of that expression to be printed on execution of that line of code.

Maynard Wright, W6PAP, was first licensed in 1957 as WN6PAP. He holds an FCC General Radiotelephone Operator's License with Ship Radar Endorsement and is a Registered Professional Electrical Engineer in California. Maynard was involved in the telecommunications industry for over 48 years and is now retired. He has served as technical editor of several telecommunications standards and holds several patents. Maynard is an ARRL member, a Life Senior Member of IEEE, a Past Chairman of the Sacramento Section of IEEE, and a Life Member and Past President of the North Hills Radio Club in Sacramento, CA.

Notes

[1]M. A. Wright, W6PAP, "Octave for Complex Characteristic Impedance", *QEX*, May/Jun., 2017, pp. 21 – 25.

[2]V. J. Young, **Understanding Microwaves**, Rider, 1960, pp. 84-87.

[3]D. T. Paris & F. Kenneth Hurd, **Basic Electromagnetic Theory**, McGraw-Hill, 1969, p. 69.

[4]W. L. Everitt, Ph.D. & G. E. Anner, M.S. in Eng., **Communication Engineering, Third Edition**, McGraw-Hill, 1956, pp. 330-332.

[5]Everitt and Anner, (*op. cit.*[4]) p. 107.

[6]R. A. Chipman, "Schaum's Outline Series - Theory and Problems of Transmission Lines," McGraw-Hill, 1968, pp. 138-139.

[7] Everitt and Anner, (*op. cit.*[4]) p. 334

[8]M. A. Wright, W6PAP, "More Octave for Transmission Lines," *QEX*, Jan./Feb., 2008, pp. 26 – 31.

[9]*The ARRL Antenna Book,* 23rd Edition. ARRL item no. 0444, available from your ARRL dealer, or from the ARRL Store, Telephone toll-free in the US 888-277-5289, or 860-594-0355, fax 860-594-0303; **www.arrl.org/shop/**; **pubsales@arrl.org**.

[10]C. Michaels, W7XC, "Complex Transmission Line Characteristic Impedance - How Important Is It?," *QST*, Nov. 1997, pp. 70-71.

Upcoming Conferences

GNU Radio Conference 2019

September 16 – 20, 2019
Huntsville, Alabama
https://www.gnuradio.org/grcon/grcon19/

The GNU Radio Conference 2019 will be held at the "Huntsville Marriott at the Space & Rocket Center." This conference celebrates and showcases the substantial and remarkable progress of the world's best open source digital signal processing framework for software-defined radios. In addition to presenting GNU Radio's vibrant theoretical and practical presence in academia, industry, the military, and among amateurs and hobbyists, GNU Radio Conference 2019 will have a very special focus.

Summer 2019 marks the 50th anniversary of NASA's Apollo 11 mission, which landed the first humans on the Moon. GNU Radio Conference selected Huntsville, Alabama, USA as the site for GNU Radio Conference 2019 in order to highlight and celebrate space exploration, astronomical research, and communication.

Space communications are challenging and mission critical. Research and development from space exploration has had and continues to have far-reaching effect on our communications gear and protocols.

Registration and an online and mobile-friendly schedule will be posted at the conference website.

ARRL and TAPR 38th Digital Communications Conference (2019)

September 20 – 22, 2019
Detroit, Michigan
www.tapr.org/dcc.html

Mark your calendar and start making plans to attend the premier technical conference of the year, the 38th Annual ARRL and TAPR Digital Communications Conference to be held September 20 – 22, 2019, in Detroit, MI. The conference location is the Detroit Metro Airport Marriott Hotel.

The ARRL and TAPR Digital Communications Conference is an international forum for radio amateurs to meet, publish their work, and present new ideas and techniques. Presenters and attendees will have the opportunity to exchange ideas and learn about recent hardware and software advances, theories, experimental results, and practical applications.

Topics include, but are not limited to: Software Defined Radio (SDR), digital voice, digital satellite communications, Global Position System (GPS), precision timing, Automatic Packet Reporting System™ (APRS), short messaging (a mode of APRS), Digital Signal Processing (DSP), HF digital modes, Internet interoperability with Amateur Radio networks, spread spectrum, IEEE 802.11 and other Part 15 license-exempt systems adaptable for Amateur Radio, using TCP/IP networking over Amateur Radio, mesh and peer to peer wireless networking, emergency and Homeland Defense backup digital communications, using Linux in Amateur Radio, updates on AX.25 and other wireless networking protocols.

Microwave Update 2019

October 3 – 5, 2019
Dallas, Texas
www.microwaveupdate.org

The North Texas Microwave Society would like to invite you to the annual Microwave Update Conference to be held October 3 – 5, 2019 at the Hilton Garden Inn and Conference Center in Lewisville (Dallas), Texas.

Microwave Update is the premier microwave conference of the year; initially started by Don Hilliard, WØPW (SK) back in 1985. This is the ideal conference to meet fellow microwave enthusiasts and share ideas and techniques that will help you conquer your next microwave band.

We have a full slate of speakers already set up. If you are interested in speaking, please let us know.

Topics will include small-dish EME, microwave propagation, parabolic-dish feedhorn design and construction, SSPAs, circuit design, latest microwave devices, software defined radios, and digital modes, just to name a few.

We still have several surplus electronics and mechanical places in the DFW area that may be worth a visit on Thursday. A workshop on GNU Radio, led by Tom McDermott, N5EG, is planned for Thursday afternoon. GNU Radio is a development and simulation environment used to create and test software defined radio applications. This is a powerful learning tool and GNU Radio can be used to implement working radio applications. Friday morning will be dedicated to "antenna gain." An informal program for the spouses has been planned, and will include local shopping and sightseeing in the Lewisville, Grapevine and greater DFW area on both Friday and Saturday.

Our Saturday night banquet speaker will be Rex Moncur, VK7MO, who has activated over 100 grid squares on 10-GHz EME in both Australia and New Zealand. Rex will show us some of the beautiful places he has visited and talk about his adventures to some of the more remote places down under. This should be a real treat for hams and spouses.

Call for papers: Kent Britain, WA5VJB, will coordinate the publishing of the proceedings by the ARRL. We are always looking for additional papers for the proceedings. You don't have to be a presenter to have your paper published in the proceedings. If you have an article on your latest microwave related project that you would like published, please send your article to Kent, WA5VJB at **wa5vjb@flashnet**.

24th Annual Pacific Northwest VHF-UHF-Microwave Conference

Issaquah, Washington
October 11 – 12, 2019
www.pnwvhfs.org

Join other weak-signal VHF, UHF and Microwave operators for the 25th Annual PNW VHF Society Conference! Details will be added to the website as they become available.

2019 AMSAT Space Symposium, 50th Anniversary

October 18 – 20, 2019
Arlington, Virginia
www.amsat.org

AMSAT announces the 2019 37th Annual AMSAT Space Symposium and General Meeting will be held on Friday through Sunday, October 18 – 20, 2019, at the Hilton Arlington, 950 North Stafford St., Arlington, VA 22203.

The Hilton Arlington is located in the heart of the Ballston neighborhood of Arlington, VA. Connected to the Ballston Metro Station, the hotel offers easy and effortless access to Washington DC's top tourist destinations like the National Mall, Smithsonian Museums, and historical monuments. The hotel is six miles from Reagan National Airport and the National Mall.

The AMSAT Board of Director's Meeting will be held just before the Symposium, October 16 – 17, at the same hotel.

The current plan includes tours of Washington DC/Baltimore area on Sunday and Monday, October 20 – 21. The banquet speakers will celebrate AMSAT's long history; an OSCAR Park display also is planned. Please plan join us for the 50th Anniversary Symposium.

You can make hotel reservations by calling the hotel directly at 703-528-6000. The group name is AMSAT, Radio Amateur Satellite Corporation. Or use the link provided on the AMSAT website.

Symposium and banquet tickets will be available for purchase on the AMSAT store beginning in July.

Build Your Go-Kit with DX Engineering!

Go-Kit Packages

DX Engineering makes it simple to assemble your perfect Go-Kit. Choose from Go-Kit combos for HF, 2 Meter or Digital operation. Packages include HF, mobile and handheld radios from leading brands; antenna tuner; speaker and mic; power supply; DC panel; battery backup switch and charger; and carrying case. Digital Go-Kits come with SignalLink™ interface and cables. Enter "Go-Kit" at DXEngineering.com for full details.

Equipment Cases

Keeping your gear safe and transportable is essential when disaster strikes. DX Engineering has rugged cases from trusted manufacturers, including iPortable's Pro2 Equipment Rack Systems that combine DC power distribution point, speaker and shelving; virtually indestructible Pro Series cases from Gator; and waterproof, watertight NANUK cases. Enter "Equipment Cases" at DXEngineering.com for the full lineup.

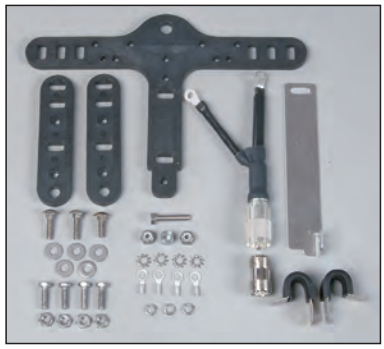

DXE-UWA213-KIT

Wire Antennas

Make us your source for wire antennas. Choose from DX Engineering's versatile EZ-BUILD UWA Center T and End Insulator Kits that let you build virtually any wire antenna type; fan dipoles from EAntenna that use multiple parallel wires with spacers to allow each band dipole to remain separate; SOTABeams' portable and pre-assembled wire antenna kits; and many more from Alpha Delta, Buckmaster and Bushcomm.

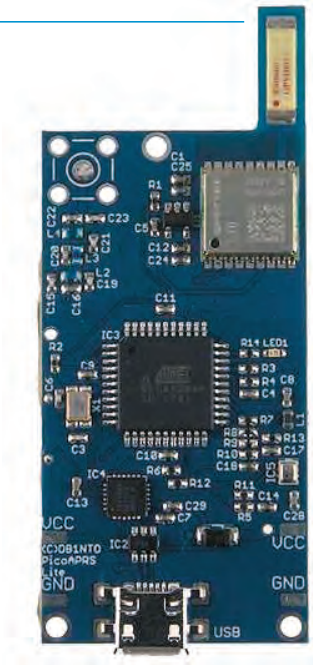

PicoAPRS-Lite APRS Transceiver Module Kit

DX Engineering now carries WIMO's incredibly versatile Automatic Packet Reporting System (APRS). Developed for balloon tracking, the PicoAPRS-Lite can also be a valuable tool for EMCOMM operations. It features automatic or manual frequency tuning, integrated GPS module with balloon mode, and temperature/air pressure sensor. It easily fits in your pocket or installs out-of-sight in your vehicle. Enter "WIMO APRS" at DXEngineering.com for more information.

ICOM YAESU KENWOOD ALINCO RigExpert Tigertronics MASTR ANT ANTENNA GUYING bhi Noise Cancellation Products

Proud sponsor of the October 2019 VP6R Pitcairn Island DXpedition

Showroom Staffing Hours:
9 am to 5 pm ET, Monday-Saturday

Ordering (via phone):
8:30 am to midnight ET, Monday-Friday
9 am to 5 pm ET, Weekends

Phone or e-mail Tech Support: 330-572-3200
8:30 am to 7 pm ET, Monday-Friday
9 am to 5 pm ET, Saturday
All Times Eastern I Country Code: +1
DXEngineering@DXEngineering.com

800-777-0703 I DXEngineering.com

FAST FREE SHIPPING over $99*

*A special handling surcharge per item applies to oversize items; truck freight fees are charged for products that are too large or too heavy for regular ground service —ask your sales rep for details.

We're All Elmers Here! Ask us at: Elmer@DXEngineering.com YouTube

YAGI URBAN BEAM

The UrbanBeam is excellent for use in high density population areas or properties with small lot sizes, where a full-sized Yagi may not be an option. The distinctive shape and small footprint (15.5 sq ft turning radius) of the UrbanBeam helps make neighbors and spouses happier, while still delivering the exceptional results you would expect of a SteppIR Yagi. The UrbanBeam is a high-performance, two element Yagi on 20m-6m and folded dipole on 40-30m. With features such as 180 degree direction change, bi-directional mode and full element retraction for stormy weather. You can enjoy all the features of a SteppIR Yagi while chasing low-sunspot-cycle DX or rag-chewing with your friends!

YAGI URBAN BEAM

GO SMALL

steppIR
COMMUNICATION SYSTEMS

DETAILS & ORDERING:

www.steppir.com

425-453-1910